Reactive microglia and cytokine release entails microtubule remodeling from acentrosomal to centrosomal arrays

Authors: #Maria Rosito[1,2], #Caterina Sanchini[1,2], Giorgio Gosti[3], Manuela Moreno[2], Simone De Panfilis[1], Maria Giubettini[4], Doriana Debellis[5], Federico Catalano[5], Giovanna Peruzzi[1], Roberto Marotta[5], Alessia Indrieri[6,7], Elvira De Leonibus[6,8], Davide Ragozzino[2,9], Giancarlo Ruocco[1,3], §Silvia Di Angelantonio[1,2*], §Francesca Bartolini[10*]

Affiliations:

[1]Center for Life Nano- & Neuro- Science, Istituto Italiano di Tecnologia, Roma, 00161, Italy.

[2]Department of Physiology and Pharmacology, Sapienza University, Rome, 00185, Italy

[3]Department of Physics, Sapienza University, Rome, 00185, Italy.

[4]Crestoptics S.p.A., Rome, 00165, Italy

[5]Electron Microscopy Facility, Istituto Italiano di Tecnologia, Genova 16163, Italy.

[6] Telethon Institute of Genetics and Medicine, Pozzuoli, 80078 Italy.

[7]Institute for Genetic and Biomedical Research, National Research Council, Milan, 20090, Italy.

[8]Institute of Biochemistry and Cellular Biology, National Research Council, Rome, 00015, Italy.

[9]Santa Lucia Foundation (IRCCS Fondazione Santa Lucia), Rome, 00179, Italy

[10]Department of Pathology and Cell Biology, Columbia University Medical Center, New York, NY 10032

*Corresponding authors Email: silvia.diangelantonio@uniroma1.it; fb2131@cumc.columbia.edu

Lead Contact: Further information and requests for resources and reagents should be directed to and will be fulfilled by the lead contact, Silvia Di Angelantonio (silvia.diangelantonio@uniroma1.it).

#These authors contributed equally.

§Senior authors

31 **Graphical abstract**

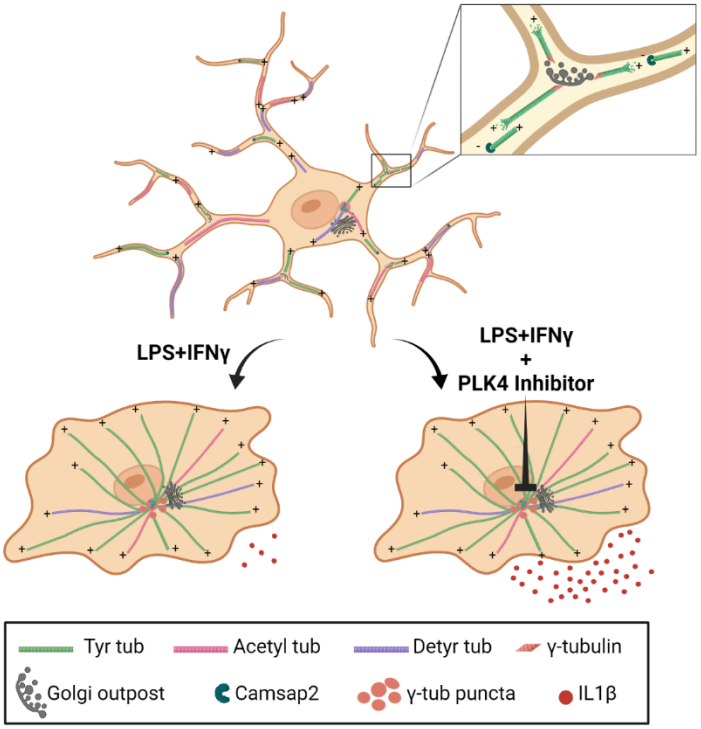

32 **Summary**

33 Microglia reactivity triggered by proinflammatory signaling entails a large-scale remodeling
34 of cellular geometry, but the role of the microtubule cytoskeleton during these changes remains
35 unexplored. Here we show that reactive proinflammatory microglia provide a heretofore unique
36 example of microtubule reorganization from a non-centrosomal array of parallel and stable
37 microtubules to a radial array of more dynamic microtubules. While in the homeostatic state
38 microglia nucleate microtubules at Golgi outposts, proinflammatory signaling induces recruitment
39 of nucleating material nearby the centrosome and inhibition of *de novo* formed pericentrosomal
40 microtubule-organizing centers enhances NLRP3 inflammasome activation and secretion of the
41 interleukin IL-1β. Our results demonstrate that remodeling of the microtubule cytoskeleton is a
42 hallmark of proinflammatory microglia reactivity and suggest that pericentrosomal microtubule
43 nucleating material maturation may offer a valuable target to modulate cytokine-mediated
44 inflammatory responses in chronic disease and tissue injury.

45

46 Running title: *Remodeling of the microtubule cytoskeleton is a hallmark of microglia reactive*
47 *states*

Keywords

Proinflammatory microglia, microtubule, centrosome, γ-tubulin, MTOC, Golgi outposts, retina, inflammation, NLRP3 inflammasome, IL-1β secretion

Introduction

Microglia are the brain's primary innate immune cells. In their homeostatic state in the healthy brain, they exhibit a ramified morphology and continuously patrol the local environment via extension and retraction of highly motile processes (Bolasco *et al.*, 2018) that act to clear cellular debris, reshape synapses, and provide neurotrophic factors (Nimmerjahn, Kirchhoff and Helmchen, 2005; Paolicelli *et al.*, 2011; Parkhurst *et al.*, 2013; Colonna and Butovsky, 2017; Basilico *et al.*, 2019; Bernier *et al.*, 2019). However, when activated by neuronal inflammation and injury, and in neurodegenerative disorders, microglia exhibit dramatically altered gene expression and morphology, displaying an amoeboid shape (Davalos *et al.*, 2005; Kettenmann *et al.*, 2011; Madry *et al.*, 2018). In this pro-inflammatory state, reactive microglia exhibit phagocytic activities that can promote tissue remodeling and if over-activated, are widely thought to contribute to brain damage and neurodegeneration (Heneka, Kummer and Latz, 2014; Colonna and Butovsky, 2017).

In eukaryotes, changes in cellular symmetry are associated with massive reorganization of both the actin and microtubule (MT) cytoskeletons. While actin and actin-based motor proteins are required for breaking the symmetry in most cells, specification of neuronal polarity depends on MTs and MT associated proteins (Li and Gundersen, 2008). Early studies suggested changes in MT spatial organization and stability also with microglia activation (Ilschner and Brandt, 1996). Despite these observations, however, only remodeling of the actin cytoskeleton has been extensively studied in microglia, and the role of the MT cytoskeleton in breaking cellular polarity during the transition from an homeostatic to a reactive state has not been explored.

MTs are intrinsically polarized polymers composed of α/β tubulin heterodimers arranged in a head to tail fashion (Nogales *et al.*, 1999). They are characterized by a fast growing plus end and a slow growing minus end that in non-neuronal cells is often attached to the centrosome, which acts as the MT organizing center (MTOC). Directional transport is enabled by the structural polarity of MTs, which is recognized by motor proteins that drive transport to either the minus end

79 (dynein) or plus end (most kinesins) (for Reviews see (Klinman and Holzbaur, 2018; Reck-
80 Peterson *et al.*, 2018). MTs are generally highly dynamic structures constantly undergoing
81 stochastic transitions from polymerization to depolymerization (catastrophe events) and vice-versa
82 (rescue events), with the two dynamic states exhibiting characteristic rates of growth or shrinkage
83 (Mitchison and Kirschner, 1984). When stabilized, MTs resist disassembly and become substrates
84 of tubulin modifying enzymes that add molecular moieties on either the α- or β-tubulin subunit.
85 The combinatorial nature of these modifications provides a "tubulin code" which controls a variety
86 of functions, including organelle transport and the mechanical properties of the MT lattice (for
87 Reviews see Janke and Bulinski, 2011; Gadadhar *et al.*, 2017; Janke and Magiera, 2020).
88 MT orientation, density, and post-translational modifications all respond and contribute to
89 breaking cellular symmetry (Etienne-Manneville, 2013; Meiring and Akhmanova, 2020).
90 Establishment of cell polarity can be achieved through centrosome repositioning or by the
91 formation of non-radial MT arrays, in which MTs are not preferentially nucleated at the
92 centrosome (Vinogradova, Miller and Kaverina, 2009; Akhmanova and Hoogenraad, 2015; Alieva
93 *et al.*, 2015). During this transition, the centrosome typically loses its maximal MT nucleating
94 activity while intracellular membranes or self-organizing assemblies of MT nucleating material
95 distant from the centrosome serve as non-centrosomal MTOCs with members of the calmodulin-
96 regulated spectrin-associated protein (CAMSAP) family often capping and stabilizing released
97 free MT minus ends (Bartolini and Gundersen, 2006; Akhmanova and Steinmetz, 2019). The local
98 stabilization of non-centrosomal MTs and relocation of the MTOCs away from the centrosome
99 and the cell center establish asymmetric MT arrays that are critical to cell differentiation.
100 We hypothesized that rearrangement of the MT cytoskeleton might be required for the
101 morphological changes that guide microglia transition from surveilling/homeostatic to reactive
102 states. Here we show that proinflammatory microglia engage a unique example of MT transition
103 from a non-centrosomal array of parallel and stable MTs in the homeostatic state to a radial array
104 of more dynamic MTs in which all MT minus ends are anchored to a pericentrosomal region. We
105 further find that in the homeostatic state, Golgi outposts are sites of non-centrosomal MT
106 nucleation, and that a pro-inflammatory challenge leads to the recruitment of pericentriolar
107 material (PCM) to the centrosome. To investigate the regulatory role of this transition we inhibited
108 the master modulator of MTOC assembly Polo-like kinase 4 (PLK4) and found that failure to
109 mature *de novo* formed pericentrosomal MTOCs increases the number of small diameter

110 extracellular vesicles (EVs) and selectively enhances IL-1β secretion. Our results unveil the unique
111 rearrangement of the MT cytoskeleton in proinflammatory microglia and indicate that
112 pericentriolar material re-localization and assembly can alone limit the release of IL-1β.
113
114 **RESULTS**
115 **Homeostatic, pro-inflammatory and anti-inflammatory primary microglia differ in MT**
116 **distribution, stability and dynamic behaviour**
117 To investigate the organization of the MT cytoskeleton in homeostatic and reactive microglia, we
118 used primary mouse microglia cultures in which the presence of ramified cells was maintained by
119 growth factors secreted by astrocytes (Bohlen *et al.*, 2017). With this approach we prepared a
120 nearly pure population of primary microglia comprised by 99% of Iba1 positive cells. To steer
121 microglia towards different reactivity states such as a pro-inflammatory or an alternatively
122 polarized microglia state (defined as anti-inflammatory), cells were challenged with either LPS-
123 IFNγ (100 ng/ml – 20 ng/ml 48 h for pro-inflammatory) or IL-4 (20 ng/ml, 48 h for anti-
124 inflammatory), and measured for the expression of their signature activation genes (Figure S1A).
125 As revealed by Iba1 staining (Figure S1B), polarized microglia underwent dramatic morphological
126 changes. We classified cell morphology as ramified (≥3 ramifications), ameboid or bipolar based
127 on number of cellular processes, cell area, and solidity, a measure of cell shape complexity (Figure
128 S1B-D). Analysis of morphology distribution under homeostatic, pro-inflammatory and anti-
129 inflammatory conditions revealed that ramified cells were enriched in untreated microglia (35 ±
130 3%) (Figure S1B and S1D), while ameboid cells represented a large majority after pro-
131 inflammatory stimulation (82 ± 3%) (Figure S1B and S1D). Conversely, when cells were
132 challenged with an anti-inflammatory stimulus, microglia mostly acquired a unipolar or bipolar
133 rod-shape morphology (54 ± 3%) characterized by the presence of a lamellipodium and a trailing
134 edge, or uropod (Figure S1B and S1D). To further detail the structural changes associated with
135 reactive microglia states *via* single-cell analyses, we chose to select for comparison only the most
136 representative morphology of each *in vitro* phenotype (ramified for homeostatic, amoeboid for
137 pro-inflammatory and bipolar for anti-inflammatory microglia).
138 We employed scanning electron microscopy (SEM) and confocal microscopy to identify
139 defined ultrastructural elements typical of each functional state (Figure S1E). Homeostatic
140 microglia exhibited many branched processes extending outward from the cell body and multiple

141 filopodia-like structures (Figure S1E) that were also positive for phalloidin staining (Figure S1H).
142 Upon pro-inflammatory challenge, microglia retracted most of their processes and acquired a
143 flattened and round morphology (Figure S1E and S1H). SEM imaging further revealed that pro-
144 inflammatory microglia displayed numerous tethered extracellular vesicles (EVs) blebbing from
145 the cell surface (Figure S1F). Analysis of EV diameter showed a bell-shaped distribution of size,
146 ranging from 250 to 650 nm (Figure S1G), consistent with microglia-shedded microvesicles (Herr
147 *et al.*, 2020). Anti-inflammatory microglia were characterized by extensive membrane ruffling at
148 both uropod and leading edge, which appeared as sheet-like structures on the dorsal cell surface
149 (Figure S1E and S1H).

150 We began to analyze the MT cytoskeleton in each microglia functional state by
151 immunofluorescence staining of tyrosinated α-tubulin (Tyr tub), a bulk tubulin marker labeling
152 the entire MT network. MTs appeared to be packed in a parallel fashion in all the cellular branches
153 extending from the cell body in both homeostatic and anti-inflammatory microglia (Figure 1A).
154 However, MTs distributed radially from a perinuclear region in pro-inflammatory microglia (Fig.
155 1A). Radial profiling of Tyr tub fluorescence intensity (Figure 1A), a measure of the distribution
156 of tubulin signal that is independent of cell shape, confirmed that MT staining was uniformly
157 distributed along the entire cell profile in homeostatic and anti-inflammatory microglia (Figure
158 1B), while in pro-inflammatory cells, Tyr tub signal rapidly decayed at increasing distances from
159 a perinuclear region (Figure 1B; exponential decay constant $k_{pro\text{-}inf} = 0.046 \pm 0.001$; $k_{homeo} = 0.013$
160 ± 0.002; $k_{anti\text{-}inf} = 0.015 \pm 0.002$).

161 To evaluate whether microglial MTs differed in stability according to their reactive state,
162 we analyzed levels and distribution of detyrosinated and acetylated tubulins, two independent
163 tubulin post-translational modifications (PTMs) associated with MT longevity (Webster and
164 Borisy, 1989; Janke and Magiera, 2020). Semiquantitative immunofluorescence analyses revealed
165 that homeostatic cells had the highest level of both detyrosinated (Figure 1C, left) and acetylated
166 (Figure 1C, right) tubulin compared to pro-inflammatory or anti-inflammatory microglia (De-
167 tyr/Tyr tub: 0.30± 0.03; 0.04 ± 0.01; 0.03 ± 0.01, Acetyl/Tyr tub: 1.02 ± 0.05; 0.69 ± 0.04; 0.72 ±
168 0.04 in homeostatic, pro-inflammatory and anti-inflammatory microglia respectively; Figure 1D),
169 suggesting that homeostatic microglia display more stable MTs.

170 We quantified the behavior of SiR-Tubulin labeled MTs (Lukinavičius *et al.*, 2014) in
171 shallow peripheral sections of the cell to measure MT plus end dynamics using time lapse wide

172 field fluorescence microcopy (Figure 1E). No change was observed among the three different
173 microglia states in rescue frequency (frequency of transitions from shrinkage to growth) or the
174 fraction of time spent in pausing or shrinkage. However, while pro-inflammatory and anti-
175 inflammatory microglia MTs exhibited a moderate yet significative drop in catastrophe frequency
176 (frequency of transitions from growth to shrinkage), they also significantly enhanced their growth
177 rates and acquired a nearly 2.5 fold increase in rates of shrinkage, resulting in an overall net rise
178 in MT dynamicity compared to MTs of homeostatic cells (0.06 ± 0.01; 0.08 ± 0.01; 0.09 ± 0.01 in
179 homeostatic, pro-inflammatory and anti-inflammatory microglia respectively; Figure 1F, Table
180 S1, Movies S1-3). In summary, and consistent with our analysis of tubulin PTMs, these data
181 suggest that microglia acquisition of pro- and anti-inflammatory phenotypes is characterized by
182 loss of MT stability and a marked increase in MT dynamics.

Fig.1

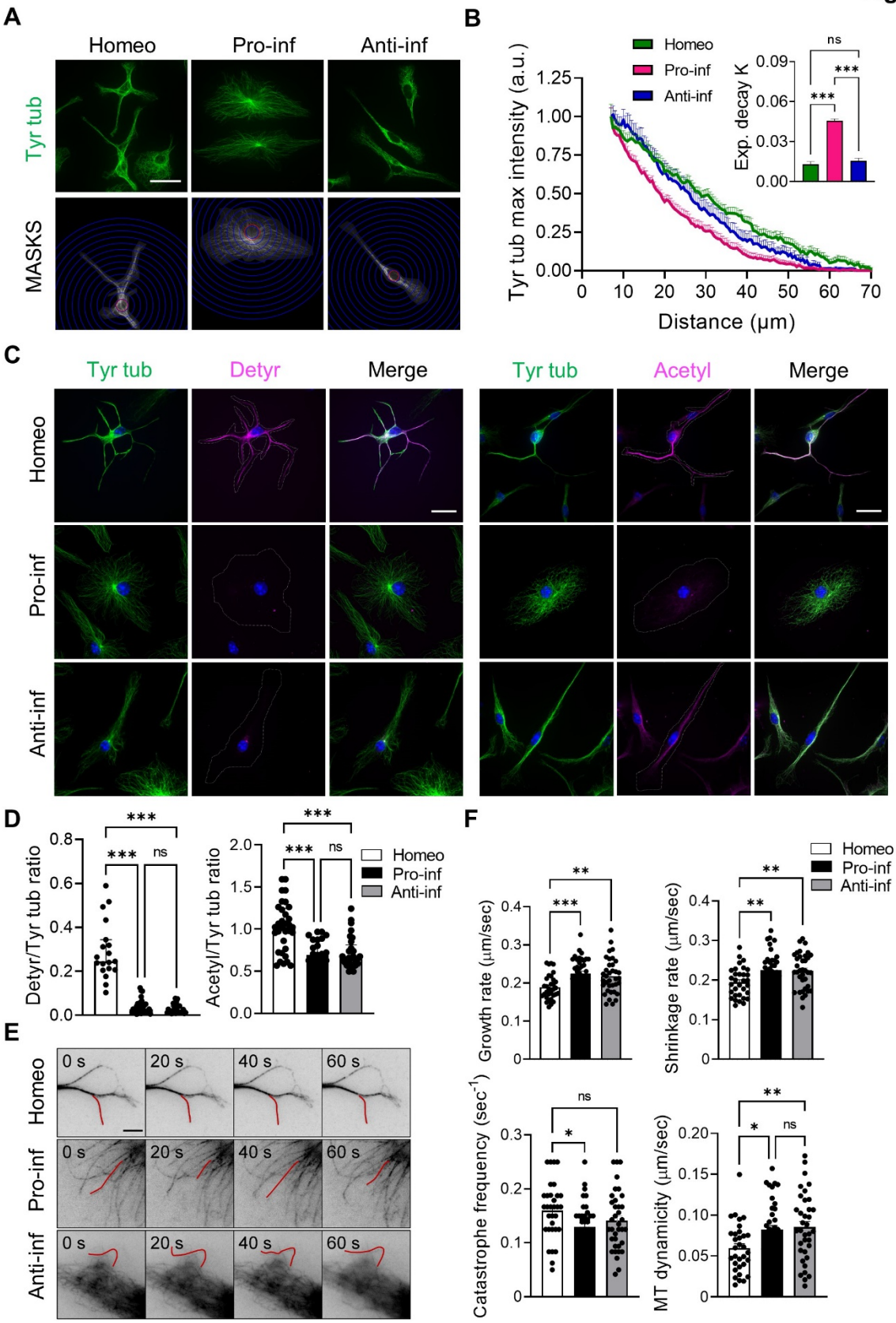
A
Homeo
Pro-inf
Anti-inf
Tyr tub
MASKS
B
Homeo
Pro-inf
Anti-inf
Tyr tub max intensity (a.u.)
Distance (µm)
Exp. decay K
ns
***
***
C
Tyr tub
Detyr
Merge
Tyr tub
Acetyl
Merge
Homeo
Pro-inf
Anti-inf
D
Detyr/Tyr tub ratio
Acetyl/Tyr tub ratio
***
***
ns
Homeo
Pro-inf
Anti-inf
E
0 s
20 s
40 s
60 s
Homeo
Pro-inf
Anti-inf
F
Growth rate (µm/sec)
Shrinkage rate (µm/sec)
Catastrophe frequency (sec-1)
MT dynamicity (µm/sec)
Homeo
Pro-inf
Anti-inf
**
***
ns
*

183

184 **Figure 1. Homeostatic, pro-inflammatory and anti-inflammatory primary microglia differ in MT**
185 **distribution, stability and dynamic behavior.**
186 **(A)** Representative images of tyrosinated α-tubulin (Tyr tub, green) staining in homeostatic (Homeo), pro-
187 inflammatory (Pro-inf) and anti-inflammatory (Anti-inf) microglia (*top*; scale bar: 20 µm) and corresponding
188 masks (MASKS) used for the analysis (*bottom*), with radial scale (unit = 5 µm; blue circles) centered at the
189 centroid of the cell nucleus. Red circle indicates the radius corresponding to the largest intensity value. **(B)** Plot
190 showing maximum fluorescence intensity values of Tyr tub vs the radial distance from cell nucleus, obtained
191 with radial profiling, in Homeo (n = 38, green), Pro-inf (n = 31, magenta) and Anti-inf (n = 38, blue) microglia.
192 Curve fit was performed using a single exponential decay function. *Insert:* bar chart reporting the exponential
193 decay constant values (K) for each condition (values are expressed as mean ± SEM from 4 independent
194 experiments; *** $p < 0.001$, One-way ANOVA – Tukey's multiple comparison test). Note faster decay of Tyr
195 tub signal in Pro-inf microglia. **(C)** Representative immunofluorescence images of Homeo, Pro-inf e Anti-inf
196 microglia showing: *left*, co-staining of Tyr tub (green) and de-tyrosinated tubulin (Detyr, magenta) (scale bar:
197 20 µm. Hoechst for nuclei visualization, blue); *right*, co-staining of Tyr tub (green) and acetylated tubulin
198 (Acetyl, magenta) (scale bar: 20 µm. Hoechst for nuclei visualization, blue). Cell outlines are indicated by white
199 dashed line. **(D)** Scatter dot plots showing immunofluorescence signal quantification of detyrosinated/
200 tyrosinated (Detyr/Tyr) tub ratio (*left*, Homeo n = 19, Pro-inf n = 32, Anti-inf n = 28 cells from 3 independent
201 experiments) and acetylated/tyrosinated (Acetyl/Tyr) tubulin ratio (*right*; Homeo n = 33, Pro-inf n = 25, Anti-
202 inf n = 29 cells from 3 independent experiments). Values are expressed as median ± interquartile range; *** $p <$
203 0.001; Kruskall-Wallis - Dunn's multiple comparisons test. Note that Pro- and Anti-inf microglia have reduced
204 tubulin PTM levels with respect to Homeo cells. **(E)** Representative inverted contrast widefield frames from
205 time lapse acquisitions of SiRtubulin in Homeo, Pro-inf and Anti-inf microglia at 4 different timepoints (0 s, 20
206 s, 40 s, 60 s). Red lines highlight MT length changes ≥ 0.5 µm between frames. Scale bar: 5 µm. **(F)** Scatter dot
207 plots representing growth rate (*top*, *left*), shrinkage rate (*top*, *right*), catastrophe frequency (*bottom*, *left*) and MT
208 dynamicity (*bottom*, *right*) in Homeo, Pro-inf and Anti-inf microglia. Values are expressed as mean ± SEM
209 (Homeo n = 30, Pro-inf n = 27 and Anti-inf n = 29 cells from 4 independent experiments). *** $p < 0.001$; ** p
210 < 0.01; * $p < 0.05$. One-way ANOVA - Dunnett's multiple comparison test.
211

212 **Homeostatic, pro-inflammatory and anti-inflammatory microglia differ in MT orientation**

213 In most dividing and motile cells, the centrosome is responsible for MT nucleation and
214 anchoring, leading to the formation of radial MT arrays in which all MT minus ends are attached
215 to the centrosome, while MT plus ends extend towards the cell periphery. In contrast, in most
216 differentiated, stationary and axially polarized cells, MTs are more stable and organized in non-
217 centrosomal arrays that are non-radially anchored at the centrosome (Bartolini and Gundersen,
218 2006).

219 We hypothesized that in microglia, the transition from the homeostatic phenotype to a
220 migrating reactive state would be paralleled by prominent changes in cell polarity driven by the
221 remodeling of MT anchoring and orientation. To test this, we analyzed the localization and
222 expression of endogenous MT plus end (EB1) and minus end (CAMSAP2) markers in
223 homeostatic, pro-inflammatory and anti-inflammatory microglia cells that had been selected
224 according to their most representative morphology (Figure 2 and S2). While EB1 is a widely
225 adopted marker of actively growing MT plus ends (comets), members of the CAMSAP family
226 regulate the formation and stability of non-centrosomal MT arrays by capping free MT minus ends
227 (Yau *et al.*, 2014; Akhmanova and Hoogenraad, 2015). Confocal immunofluorescence analysis
228 showed that in pro-inflammatory and anti-inflammatory microglia, EB1 decorated most free MT
229 ends (Tyr tub stained) (pro-inflammatory, 88%; anti-inflammatory, 82%) that extended towards
230 the cell periphery (Figure 2A), confirming the existence of a prominent pool of dynamic MTs
231 arranged radially with their minus ends attached to a perinuclear region of the cell. EB1 comets
232 were also clearly visible at MT ends in homeostatic microglia although to a lesser extent
233 (homeostatic 63% of MTs $p < 0.001$, see Figure S2A for contingency analysis). Western blot
234 analysis of whole cell lysates showed that total EB1 protein levels did not change in reactive
235 microglia compared to homeostatic cells (Figure S2B). However, a detailed measurement of
236 fluorescence intensity gradients of EB1 positive comets with respect to the location of the cell
237 nucleus (Figure 2B, arrows) identified distinct MT polarity patterns, with anterograde and
238 retrograde orientation. Specifically, a population of retrograde comets was observed in
239 homeostatic and anti-inflammatory microglia as opposed to pro-inflammatory microglia in which
240 all the comets were oriented away from the cell nucleus and toward the cell periphery (23.4%,
241 12.5% and 0.5%, respectively; $p < 0.001$ Figure S2C). Detection of a pool of retrograde comets in
242 homeostatic microglia suggested the presence of non-centrosomal MT arrays, which we
243 investigated by analyzing the expression and subcellular distribution of endogenous CAMSAP2.
244 Western blot analysis of whole cell lysates revealed endogenous expression of CAMSAP2 in all
245 three microglia phenotypes, with higher protein content in homeostatic microglia (Figure S2D).
246 However, while in homeostatic and anti-inflammatory cells CAMSAP2 often distributed to
247 isolated and clustered puncta along cell ramifications (Figure 2C, and 2D arrows), cytosolic
248 CAMSAP2 signal was detectable only around the perinuclear region in pro-inflammatory
249 microglia (Figure 2C and 2D). Radial profiling of CAMSAP2 fluorescence intensity (Figure 2E),

250 used as a measure of CAMSAP2 distribution in the cytosol, confirmed that CAMSAP2 signal
251 decayed more rapidly at increasing distances from the perinuclear region in pro-inflammatory
252 microglia than in homeostatic and anti-inflammatory cells (Figure 2E, and insert).

253 Altogether, these data indicate that homeostatic and anti-inflammatory microglia display a
254 mixed MT polarity pattern resembling neuronal MTs in dendrites and that the acquisition of a pro-
255 inflammatory phenotype represents a unique example of remodeling of the MT cytoskeleton from
256 an array of parallel non-centrosomal MTs to a radial array of MTs all anchored to pericentrosomal
257 MTOCs through their minus ends.

Fig.2

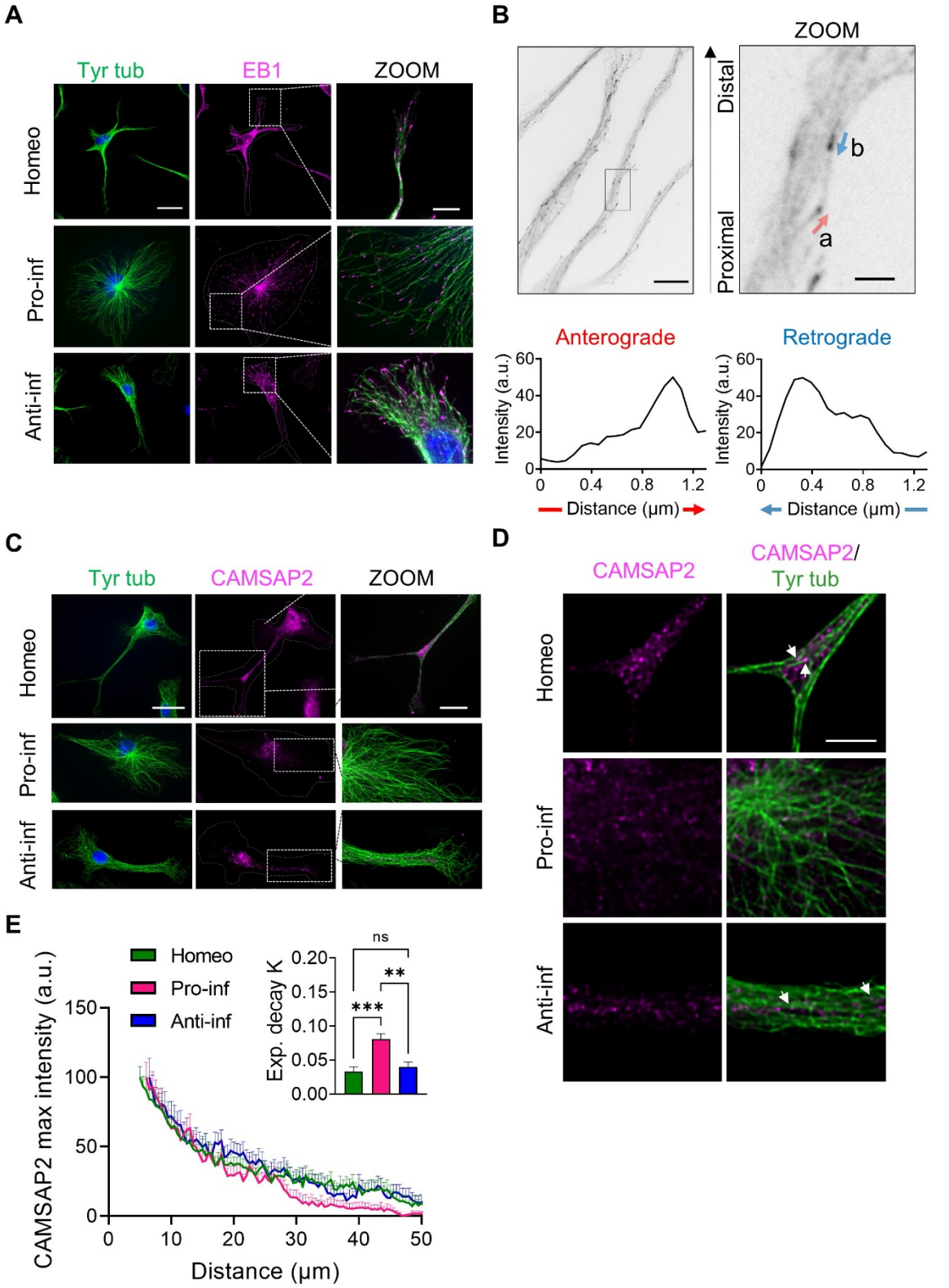
A
Tyr tub
EB1
ZOOM
Homeo
Pro-inf
Anti-inf
B
ZOOM
Distal
Proximal
b
a
Anterograde
Retrograde
Intensity (a.u.)
Distance (μm)
C
Tyr tub
CAMSAP2
ZOOM
D
CAMSAP2
CAMSAP2/
Tyr tub
E
Homeo
Pro-inf
Anti-inf
CAMSAP2 max intensity (a.u.)
Distance (μm)
Exp. decay K
ns
**
***

258

259 **Fig. 2. Homeostatic, pro-inflammatory and anti-inflammatory primary microglia differ in MT**
260 **orientation. (A)** Representative immunofluorescence images of EB1(magenta) and tyrosinated α-tubulin (Tyr
261 tub) (green) in homeostatic (Homeo), pro-inflammatory (Pro-inf) and anti-inflammatory (Anti-inf) microglia.
262 (Scale bar: 20 μm; zoom: 5 μm. Hoechst for nuclei visualization, blue). Cell outlines are indicated by white
263 dashed line. **(B)** Representative inverted contrast single plane image of EB1 immunofluorescence (*top*, *left*. Scale
264 bar 10 μm). Direction of EB1 signal gradient relative to the cell nucleus was used to identify EB1 anterograde
265 (a, red arrow) and retrograde (b, blue arrow) comets (*top*, *right*; scale bar: 2 μm). Bottom: intensity profile of
266 anterograde (left) and retrograde (right) comets. **(C)** Representative z-projection confocal images showing
267 CAMSAP2 (magenta) and Tyr tub (Green) signal in Homeo, Pro-inf and Anti-inf microglia. Cell outlines are
268 indicated by white dashed line (scale bar: 20 μm; zoom: 5 μm. Hoechst for nuclei visualization, blue). **(D)** Single
269 confocal planes at higher magnification of CAMSAP2 (magenta) and Tyr tub (Green) signal in Homeo, Pro-inf
270 and Anti-inf microglia. Scale bar: 5 μm. Note that CAMSAP2 signal is present in microglia processes in Homeo
271 and Anti-inf cells. **(E)** Plot showing maximum fluorescence intensity values of CAMSAP2 vs the radial distance
272 from cell nucleus, obtained with radial profiling, in Homeo (n = 18 cells, green), Pro-inf (n = 14 cells, magenta)
273 and Anti-inf (n = 19 cells, blue) microglia. Curve fit was performed using single exponential decay function.
274 Insert: bar chart reporting the exponential decay constant values (K) for each condition (values are expressed as
275 mean ± SEM from 4 independent experiments; *** $p < 0.001$, ** $p < 0.01$ One-way ANOVA – Tukey's multiple
276 comparison test.
277

278 **Homeostatic microglia nucleate non-centrosomal MTs from Golgi outposts**

279 CAMSAP2 is necessary for the tethering of newly nucleated non-centrosomal MT minus
280 ends during the establishment of polarity in many cell types (Tanaka *et al.*, 2012; Yau *et al.*, 2014;
281 Martin *et al.*, 2018). We investigated the distribution of γ-tubulin, the major MT nucleator in
282 eukaryotic cells, in homeostatic and reactive microglia by confocal microscopy and found that
283 while in homeostatic and anti-inflammatory cells γ-tubulin displayed a punctate distribution
284 around the perinuclear region and along cellular processes, in pro-inflammatory microglia γ-
285 tubulin signal was restricted to the centrosomal and pericentrosomal area (Figure 3A, Figure S3A
286 and Figure 4 and S4). Radial profiling (Figure 3B) of γ-tubulin fluorescence intensity, used as a
287 measure of γ-tubulin signal distribution in the cell, confirmed that γ-tubulin signal decayed more
288 rapidly at increasing distances from the perinuclear region in pro-inflammatory microglia
289 compared to homeostatic and anti-inflammatory cells (Figure 3B, and insert). This observation
290 was confirmed by the analysis of γ-tubulin signal over the cell area (Figure S3B) and detection of

291 higher γ-tubulin levels in homeostatic and anti-inflammatory microglia compared to pro-
292 inflammatory cells (Figure S3C).

293 Altogether, these data demonstrate that the acquisition of a pro-inflammatory phenotype is
294 characterized by restricted localization of γ-tubulin to a pericentrosomal area, which is necessary
295 to establish radial MT arrays. The presence of γ-tubulin in cell ramifications of homeostatic
296 microglia further suggests that microglia are alternatively enriched in non-centrosomal MT
297 nucleation sites, which are necessary to establish non-centrosomal MT arrays.

298 Golgi outposts can serve as acentrosomal MTOCs in other highly polarized brain cells,
299 such as neurons and oligodendrocytes, (Ori-McKenney, Jan and Jan, 2012; Fu *et al.*, 2019;
300 Valenzuela *et al.*, 2020). We thus analyzed the distribution of the Golgi marker GM130, a
301 scaffolding protein peripherally associated with Golgi membranes and a marker of Golgi outposts
302 (Wu and Akhmanova, 2017). Co-staining of GM130 with tyrosinated tubulin (Tyr tub)
303 demonstrated that the presence of Golgi outposts is a feature of homeostatic microglia, and that
304 their presence was dramatically reduced in pro-inflammatory cells (Figure 3C and 3D).
305 Importantly, most of the isolated GM130 positive mini-stacks (73.6%) were decorated by γ-tubulin
306 (Figure 3E). To determine whether Golgi outposts could function as MTOCs in homeostatic
307 microglia, MT nucleation was evaluated *in situ* by analyzing MT re-nucleation after nocodazole
308 washout (Figure S3D). We found that both at 15 and 120 mins after nocodazole washout to allow
309 MT-regrowth after nocodazole-induced MT depolymerization, MTs (stained with Tyr tub)
310 emerged from Golgi membranes (GM130 positive) both at pericentrosomal sites and at Golgi
311 outposts located far from the centrosome (Figure 3F). Importantly, γ-tubulin was localized to
312 nucleation-competent Golgi outposts, indicating that non-centrosomal MT re-nucleation did not
313 occur spontaneously at these sites but was strictly dependent on the presence of a γ-tubulin
314 nucleation complex (Figure 3E).

315 These data demonstrate that in homeostatic microglia Golgi outposts can function as sites
316 of acentrosomal MT nucleation and suggest that γ-tubulin-dependent non-centrosomal nucleation
317 is necessary to establish an asymmetric MT array in these cells.

318 To assess whether these *in vitro* observations were representative of MT nucleation in
319 microglia residing in tissue, we analyzed the subcellular distribution of GM130 in retinal
320 microglia: retina and brain share a common embryological origin and similar cell types (Sernagor,
321 Eglen and Wong, 2001; Kavcic, Vaughn and Duffy, 2011; Chang *et al.*, 2014; Lee *et al.*, 2014;

322 Bambo *et al.*, 2015; Javaid *et al.*, 2016). Moreover, retinal neurons are arranged in distinct layers,
323 and microglia are usually restricted to the retinal ganglion cell layer, thus offering an accessible
324 structure for the imaging of their MT cytoskeleton. To identify the microglial cytoskeleton in retina
325 we used cx3cr1$^{gfp/+}$ mice, which constitutively express GFP in microglia. As expected, retinal
326 microglia from control cx3cr1$^{gfp/+}$ mice displayed a highly ramified morphology (Figure S3E),
327 typical of homeostatic surveillant cells (Grimaldi *et al.*, 2018; Basilico *et al.*, 2019; Cordella *et al.*,
328 2021). More importantly, confocal immunofluorescence analysis of GM130 signal in retinal GFP
329 positive microglia confirmed the presence of isolated Golgi outposts also in the processes of
330 homeostatic microglia residing in tissue (5 ± 1 per cell, n = 11; Figure 3G, S3F and S3G).
331 Altogether, these results support the notion that MT organization in homeostatic microglia
332 resembles the MT architecture typical of highly polarized, terminally differentiated cells and
333 strongly suggest that γ-tubulin dependent non-centrosomal MT nucleation at Golgi outposts is a
334 *bona fide* feature of homeostatic, surveilling microglia *in vitro* and *in vivo*.

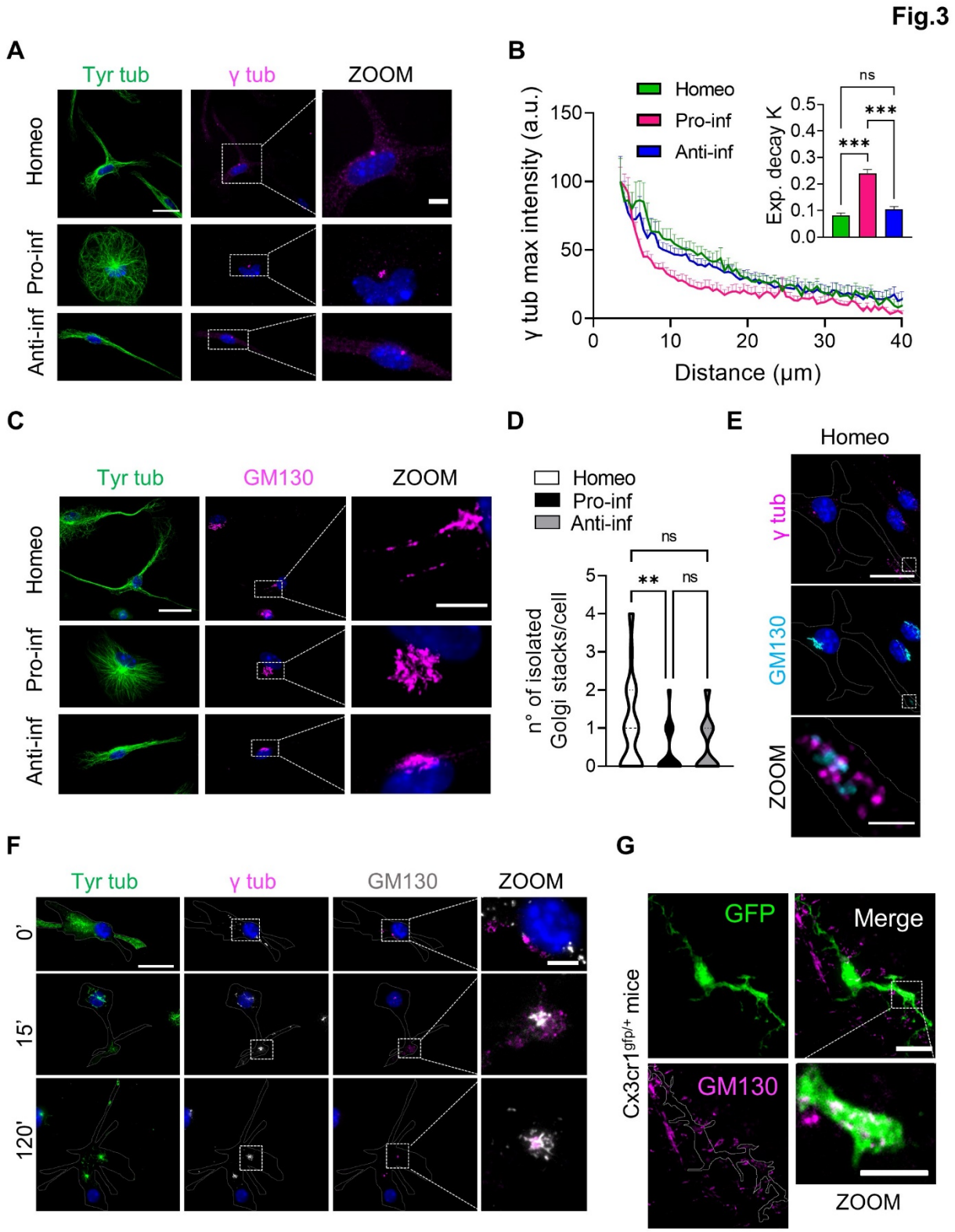

Fig. 3. Homeostatic microglia nucleate non-centrosomal MTs from Golgi outposts. (A) Representative images of homeostatic (Homeo), pro-inflammatory (Pro-inf) and anti-inflammatory (Anti-inf) microglia stained

338 for tyrosinated α-tubulin (Tyr tub, green) and γ-tubulin (γ tub, magenta; scale bar: 20 μm; zoom: 5 μm. Hoechst
339 for nuclei visualization, blue). **(B)** Plot showing maximum fluorescence intensity values of γ tub vs the radial
340 distance from cell nucleus, obtained with radial profiling, in Homeo (n = 13 cells, green), Pro-inf (n = 14 cells,
341 magenta) and Anti-inf (n = 14 cells, blue) microglia. Curve fit was performed using single exponential decay
342 function. Insert: bar chart reporting the exponential decay constant values (K) for each condition (values are
343 expressed as mean ± SEM from 3 independent experiments; *** $p < 0.001$, One-way ANOVA – Tukey's
344 multiple comparison). Note faster decay of γ-tub signal in Pro-inf microglia. **(C)** Representative confocal images
345 showing co-staining of tyrosinated tubulin (Tyr tub) (green) and GM130 (magenta) in Homeo, Pro-inf and Anti-
346 inf microglia (scale bar: 20 μm; zoom: 5 μm. Hoechst for nuclei visualization, blue). **(D)** Violin plot showing
347 number of isolated Golgi stacks per cell in the three phenotypes. Values are expressed as mean ± SEM of Homeo
348 n = 57, Pro-inf n = 34 and Anti-inf n = 36 cells from 3 independent experiments. ** $p < 0.01$. Kuskall-Wallis -
349 Dunn's multiple comparison test. **(E)** Representative images showing GM130 (cyan) and γ-tub (magenta)
350 staining in Homeo microglia. (Scale bar: 20 μm; zoom: 2 μm. Hoechst for nuclei visualization, blue). Note the
351 presence of Golgi outposts in microglia processes. **(F)** Representative confocal images of the time course of the
352 MT re-nucleation assay after nocodazole washout in Homeo microglia stained for Tyr tub (green), GM130 (gray)
353 and γ tub (magenta). Scale bar: 20 μm; zoom: 5 μm. Hoechst for nuclei visualization, blue). Time 0' represents
354 the MT depolymerizing effect of nocodazole in homeostatic cells without free tubulin extraction. Note that MTs
355 nucleate from distal Golgi outposts that are positive for γ-tubulin. **(G)** Representative z-projection confocal
356 images of retinal slices (50 μm thickness) from $cx3cr1^{gfp/+}$ mice, expressing GFP in microglia cells, stained with
357 GM130 (magenta) to visualize Golgi outposts. Scale bar: 5 μm. Zoom is a single confocal plane of a microglia
358 ramification stained for GM130; scale bar: 5 μm.
359

360 **Pericentrosomal redistribution of microtubule-nucleating material is a hallmark of pro-**
361 **inflammatory microglia and regulates IL-1β secretion**

362 The recruitment of pericentriolar material (PCM) to the centrosome has been described as
363 a functional step for macrophage activation upon pro-inflammatory stimuli (Vertii *et al.*, 2016).
364 We thus investigated whether the recruitment of γ-tubulin to a pericentrosomal area was also a
365 hallmark of pro-inflammatory microglia.

366 As revealed by super-resolution microscopy, pro-inflammatory microglia exhibited
367 multiple γ-tubulin$^+$ puncta that localized to a perinuclear region (Figure 4A). Quantification of the
368 number of γ-tubulin$^+$ puncta indicated that most pro-inflammatory cells had more than 3 puncta
369 (70 ± 10%; Figure 4B). Conversely, almost all homeostatic and anti-inflammatory microglia
370 displayed only 1 or 2 γ-tubulin$^+$ puncta (95 ± 3% and 96 ± 2%, respectively; Figure 4B). γ-tubulin

371 localization to pericentrosomal puncta showed a time-dependent increase of both number and
372 fluorescence integrated density upon LPS-INFγ challenge (Figure 4C and 4D) and the recruitment
373 of γ-tubulin$^+$ puncta was dependent on a dynamic MT cytoskeleton because a low dose of taxol
374 was sufficient to inhibit it (Figure S4A and S4B). Notably, in most pro-inflammatory cells with
375 >2 γ-tubulin$^+$ puncta (65 ± 10%; Figure S4C) the centrosomal marker centrin-3 localized only to
376 ≤2 γ-tubulin$^+$ puncta. In addition, while a quarter of pro-inflammatory cells was proliferating (23
377 ± 4%; Figure S4E and S4F), most pro-inflammatory microglia displayed >2 γ-tubulin$^+$ puncta (70
378 ± 10%; Figure 4B) and ≤ 2 centrin$^+$ puncta (Figure S4D). Conversely, PCM localization to γ-
379 tubulin$^+$ puncta was confirmed in most puncta by coimmunostaining with pericentrin (86 ± 5% of
380 colocalizing puncta), a conserved PCM scaffold protein necessary for MTOC assembly and
381 maturation (Zimmerman *et al.* 2004 Figure S4G), and both centrin$^+$ and centrin$^-$ γ-tubulin$^+$ puncta
382 localized to the center of MT asters (Fig. S4H), indicating that γ-tubulin reorganization in pro-
383 inflammatory microglia is ascribed to PCM maturation that is uncoupled from cell or centrosome
384 duplication and that *de novo* generated PCM puncta act as MTOCs.
385 Perinuclear γ-tubulin redistribution was also observed in proinflammatory microglia in a
386 mouse model of retinal inflammation. For this, we took advantage of a well-established protocol
387 of acute inflammatory uveitis (Becker *et al.*, 2001; Rosenbaum *et al.*, 2011; Wang *et al.*, 2011;
388 Chu *et al.*, 2016; Bell *et al.*, 2020; Wu *et al.*, 2020) induced by intravitreal injection of LPS (Figure
389 S5A) to activate retinal microglia towards the pro-inflammatory phenotype. Microglia residing in
390 retinal slices from LPS-treated mice acquired an amoeboid morphology with reduced branching
391 complexity, as revealed by skeleton analysis of Iba1 positive cells (Figure S5B and S5C).
392 Moreover, co-immunolabelling with Iba1 and γ-tubulin demonstrated that while in control (sham)
393 mice retinal microglia displayed punctate diffuse γ-tubulin staining along cellular ramifications
394 (Figure 4E), in LPS treated mice microglia clearly exhibited a condensed γ-tubulin pattern,
395 clustered around a perinuclear region (Figure 4E). This was confirmed by quantitative analysis of
396 γ-tubulin signal over the cell area and of the number of γ-tubulin$^+$ puncta per cell (Figure 4F).
397 In summary, these data indicate that the presence of pericentrosomal MTOC maturation is a
398 *bona fide* feature of pro-inflammatory microglia *in vitro* and *in vivo*.
399

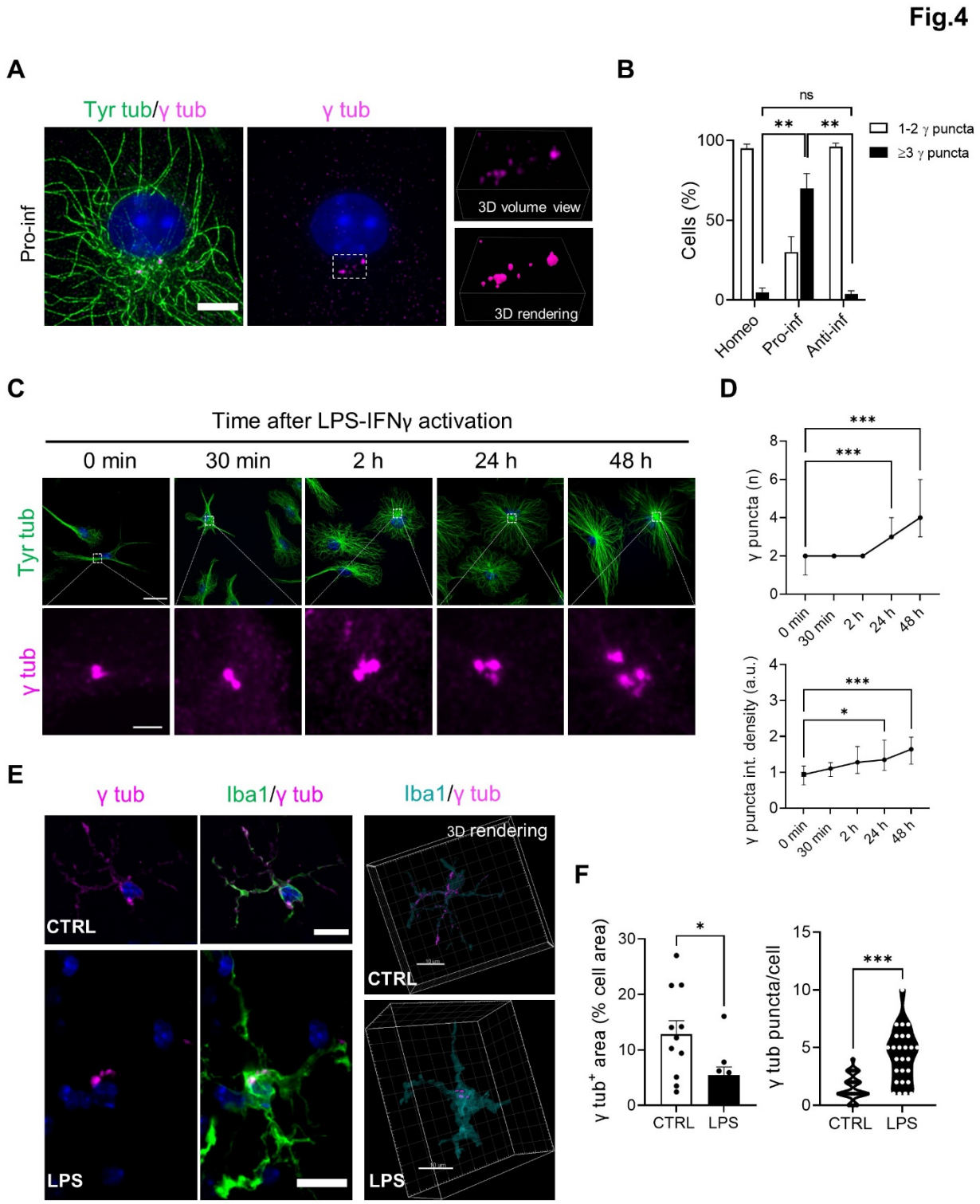

Fig 4. Redistribution of pericentriolar material is a hallmark of pro-inflammatory microglia *in vitro* and *in vivo*. (A) Representative confocal images showing γ-tubulin (γ tub) puncta (magenta) and tyrosinated α-tubulin (Tyr Tub, green) immunolabeling in pro-inflammatory (Pro-inf) microglia (*left*, *middle*). Scale bar: 5

404 µm. Hoechst for nuclei visualization, blue. *Right:* relative volume view *(top)* and 3D rendering *(bottom)* of γ tub
405 puncta (magenta) acquired via structured illumination microscopy. **(B)** Bar chart reporting the percentage of
406 cells displaying 1-2 γ tub puncta (white bars) or >3 γ tub puncta (black bars) in homestatic (Homeo), pro-
407 inflammatory (Pro-inf) and anti-inflammatory (Anti-inf) microglia. Values are expressed as mean ± SEM from
408 3 independent experiments. ** $p < 0.01$. One-way ANOVA - Dunnett's multiple comparison test. **(C)** Time
409 course of γ -tubulin (γ tub) redistribution during the process of microglia pro-inflammatory activation:
410 representative images showing γ tub (magenta) and tyrosinated α -tubulin (Tyr tub, green) staining at different
411 time points (0 min, 30 min, 2 h, 24 h, 48 h). Scale bar: 20 µm; zoom, 2 µm. Hoechst for nuclei visualization,
412 blue. **(D)** Time course of the number of γ puncta per cell (top) and the quantification of γ puncta fluorescence
413 intensity (bottom) during the process of microglia pro-inflammatory activation. Values are expressed as median
414 ± interquartile range (T0 n = 32; T30 min n = 40; T2h n = 44; T24h n = 41; T48h n = 33; from 3 independent
415 experiments); *** $p < 0.001$; ** $p < 0.01$; * $p < 0.05$, Kruskal-Wallis test - Dunn's multiple comparison test
416 respect to T0. **(E)** *Right*: representative maximum intensity projections of retinal slices (50 µm thickness) from
417 control (CTRL) mice stained for γ tub (magenta) and Iba-1 (green) antibodies (Scale bar: 10 µm. Hoechst for
418 nuclei visualization, blue). *Left*: 3D rendering of same retinal microglia highlighting the intracellular distribution
419 of γ tub in CTRL (sham) and LPS treated mice. Scale bar: 10 µm. **(F)** *Left*: scatter dot plot showing the γ tub
420 signal over the cell area of retinal microglia from CTRL (sham) and LPS treated mice. Values are expressed as
421 mean ± SEM of n = 11/3 cells/mice (CTRL) and n = 9/3 cells/mice (LPS). * $p < 0.05$. Student's t-test. *Right*:
422 violin plot showing the number of γ tub puncta per microglia in retinal slices from CTRL and LPS treated mice
423 of n = 28/3 cells/mice (CTRL) and n = 26/3 cells/mice (LPS). *** $p < 0.001$, Student's t-test.
424

425 Next, we examined if maturation of pericentrosomal MTOCs was a regulatory step for
426 microglia acquisition of the pro-inflammatory phenotype. To this end, we treated microglia with
427 the selective PLK4 inhibitor centrinone to hamper PCM maturation (Yang et al., 2020) prior to
428 LPS-INFγ stimulation (Figure 5A) and measured its effects on EV blebbing and cytokine release
429 (Figure 5). First, we found that centrinone increased the number (4.7-fold; Figure 5C, top) and
430 reduced the diameter (by 30%; Figure 5C, bottom) of EVs blebbing from the cell surface of pro-
431 inflammatory microglia (Fig. 5A-C). It is acknowledged that the activation of NLRP3-
432 inflammasome is a characteristic feature of pro-inflammatory microglia and macrophages
433 (Schroder and Tschopp, 2010; Davis, Wen and Ting, 2011; Latz, Xiao and Stutz, 2013; Gustin *et*
434 *al.*, 2015; Hanslik and Ulland, 2020) and that the centrosome-associated protein kinase NEK7 is
435 required for NLRP3–inflammasome activation (for review see Seoane *et al.* 2020). In addition,
436 NLRP3 activation is required for IL-1β maturation in immortalized and primary microglia (Gustin
437 *et al.*, 2015; Ji *et al.*, 2021), and inhibition of PLK4 leads to NLRP3 hyper-activation through

438 NEK7 dephosphorylation in bone marrow-derived macrophages (Yang *et al.*, 2020). We then
439 measured NLRP3-inflammasome protein levels in homeostatic and pro-inflammatory microglia
440 upon centrinone treatment. We found that in homeostatic microglia, LPS-IFNγ but not centrinone
441 alone increased NLRP3 expression while centrinone / LPS-IFNγ co-treatment enhanced NLRP3
442 more than LPS-IFNγ alone (Figure 5D), suggesting that inhibition of PCM maturation induces
443 NLRP3 hyperactivation in pro-inflammatory microglia. We investigated whether PLK4 inhibition
444 modulates microglia IL-1β release and found that co-treatment with centrinone enhanced pro-
445 inflammatory microglia-mediated IL-1β release, without affecting IL-1β release from homeostatic
446 cells (Figure 5E). In addition, we observed that centrinone did not modulate the release of IL-10
447 and IL-6 (Figure 5F), indicating that PLK4 inhibition enhances pro-inflammatory microglia IL-
448 1β release through NLRP3-inflammasome activation but has no effect on NLRP3-independent
449 pathways.
450 Together, these data demonstrate that microglia pro-inflammatory reactivity induces PCM
451 maturation *in vivo* and *in vitro*, and that this step is a negative regulator of NLRP3-dependent IL-
452 1β release. They also indicate that remodeling of the MT cytoskeleton during pro-inflammatory
453 reactivity is functionally coupled to the regulation of cytokine release, providing a novel potential
454 target of microglia treatment in inflammatory diseases.

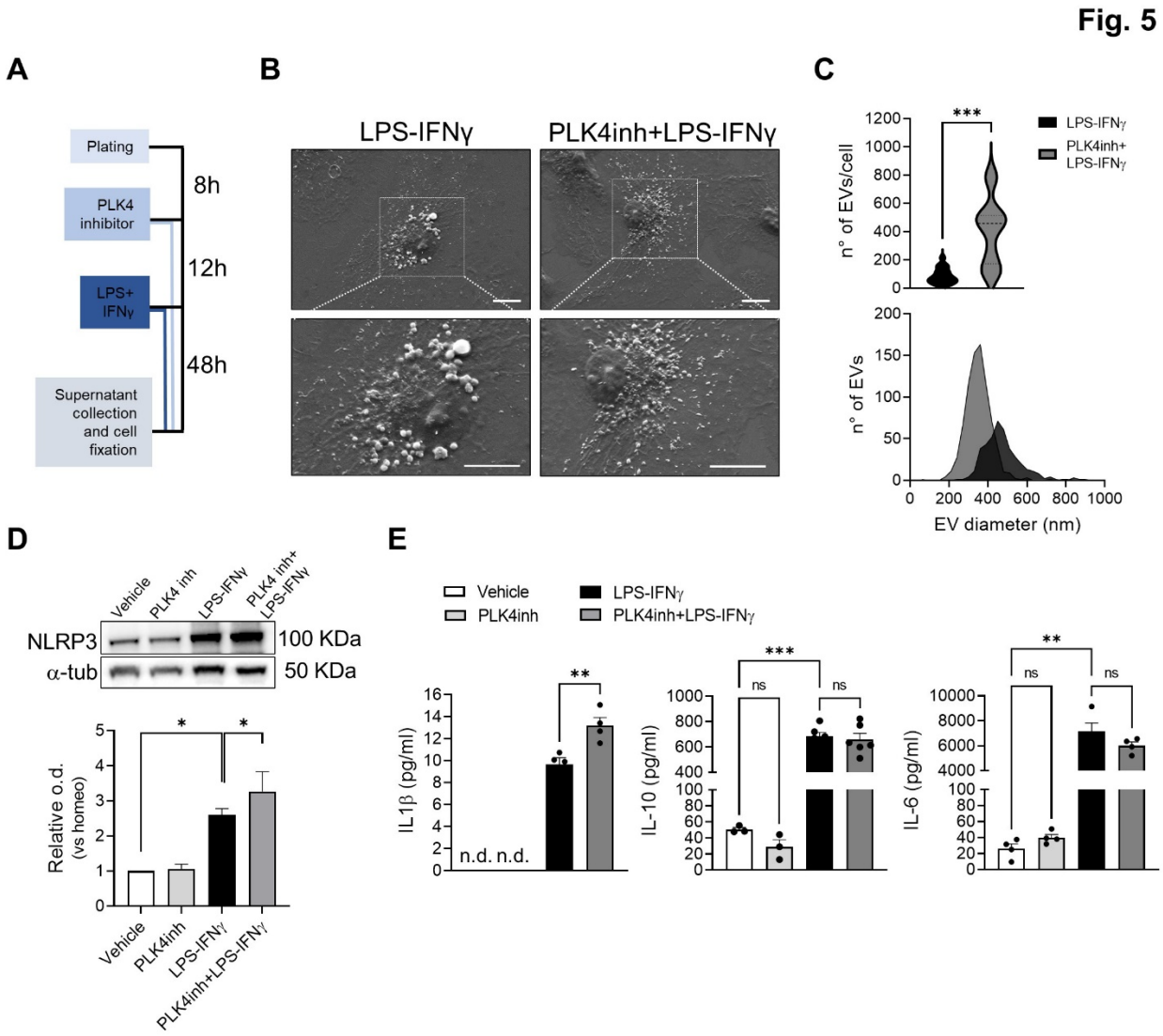

Fig 5. Inhibition of pericentriolar material maturation induces NLRP3 inflammasome hyperactivation in pro-inflammatory microglia

(A) Experimental timeline of PLK4 inhibitor treatment and pro-inflammatory cytokine administration. **(B)** p < **(B)** Scanning electron micrographs showing extracellular vesicles (EVs) on the surface of LPS-IFNγ (*left*) and PLK4 inhibitor+LPS-IFNγ (*right*). Scale bar: 10 µm. **(C)** *Top*: violin plot showing the number of EVs in Pro-inf microglia with or without PLK4inh treatment (LPS-IFNγ n = 17 cells, PLK4 inhibitor+LPS-IFNγ n = 19 cells from 2 independent cultures; *** $p < 0.001$, Student's t-test). *Bottom*: distribution of EV size measured on cell surface of LPS-IFNγ and PLK4 inhibitor+LPS-IFNγ microglia (LPS-IFNγ n = 17 cells, PLK4 inhibitor+LPS-IFNγ n = 19 cells). **(D)** *Bottom*: bar chart reporting the amount of NLRP3 protein level in Vehicle, PLK4 inhibitor, LPS-IFNγ and PLK4 inhibitor+LPS-IFNγ microglia; *top*: representative immunoblot of NLRP3. Values are expressed as median ± interquartile range from 4 independent experiments, * $p < 0.05$, Mann Whitney

467 test. **(E)** Scatter dot plot showing protein quantification by ELISA of *left*: IL1β (n = 4 independent experiments,
468 n.d. = non detectable), *middle*: IL-10 (Vehicle n = 3, PLK4inh n = 3, LPS-IFNγ n = 5 and PLK4 inhibitor+LPS-
469 IFNγ n = 5 independent experiments) and *right*: IL-6 (n = 4 independent experiments). Values are expressed as
470 mean ± SEM. For IL-1β: ** $p < 0.01$, Student's t-test. Note that supernatants from both Vehicle and PLK4
471 inhibitor microglia have undetectable levels of cytokine. For IL-10 and IL-6: *** $p < 0.001$, ** $p < 0.01$; One-
472 way ANOVA - Holm-Šídák's multiple comparison test.
473

474 **Discussion**

475 Here we describe the reorganization of the microglial MT cytoskeleton that characterizes
476 the transitions between homeostatic, pro-inflammatory and anti-inflammatory states, and
477 demonstrate the functional interplay between microglial PCM maturation and pro-inflammatory
478 reactivity. Our findings demonstrate that pro-inflammatory microglia reactivity orchestrates a so
479 far unique rearrangement of the MT cytoskeleton from a non-centrosomal array of parallel and
480 stable MTs nucleated at Golgi outposts characteristic of the homeostatic state, to a radial array in
481 which MTs are anchored to *de novo* formed pericentrosomal MTOCs through their minus ends.
482 Through detailed *in vitro* phenotyping and *in vivo* validation, we report four main findings
483 summarized in our Graphical Abstract. 1) Homeostatic microglia possess stable MT arrays, while
484 microglia reactivity increases MT dynamic behavior. 2) Non-centrosomal MT organization in
485 arrays with mixed polarity is a feature of homeostatic microglia, similar to the architecture typical
486 of highly specialized cells such as neurons and oligodendrocytes. 3) Pro-inflammatory microglia
487 reactivity results in restricted γ-tubulin localization to puncta around the centrosome because of *de*
488 *novo* PCM maturation. 4) PCM maturation in pro-inflammatory microglia is a regulator of
489 NLRP3-dependent IL-1β release.

490 To date, only circumscribed evidence has suggested that ramified microglia possess more
491 acetylated and detyrosinated MTs than ameboid pro-inflammatory cells (Ilschner and Brandt,
492 1996; Yu *et al.*, 2018). Here, we show that homeostatic ramified microglia display higher levels
493 of tubulin acetylation and detyrosination, two indirect indicators of "older", i.e., more stable and
494 less dynamic, MT subpopulations (Webster and Borisy, 1989; Baas *et al.*, 2016). Moreover, we
495 report that during classical and alternative activation obtained with either LPS-IFNγ or IL-4
496 stimulation respectively (Gordon and Taylor, 2005; Perry, Nicoll and Holmes, 2010; Durafourt *et*
497 *al.*, 2012), microglia MTs become less stable and more dynamic, suggesting that the acquisition

498 of new cellular functions induces changes in MT stability *via* modulation of MT dynamics (Li and
499 Yang, 2015).

500 We describe that homeostatic/ramified microglial MTs exhibit an asymmetric dendrite-like
501 organization characterized by EB1 comets arranged in mixed polarity with the minus-end capping
502 protein CAMPSAP2 localized at branching points and cell ramifications. In anti-inflammatory
503 microglia, we find lower levels of CAMSAP2 that localize in a similar fashion in bipolar processes.
504 The presence of CAMSAP2 in microglia processes might suggest that, as in neurons (Burton and
505 Paige, 1981; Heidemann, Landers and Hamborg, 1981; Baas *et al.*, 1988, 1991; Jiang *et al.*, 2014;
506 Yau *et al.*, 2014), stabilization of non-centrosomal MTs at their minus ends is important to achieve
507 elongated bipolar morphology, typical of anti-inflammatory microglia, and for the formation of
508 long branched cellular processes patrolling brain parenchyma in homeostatic microglia.

509 We find that the acquisition of a pro-inflammatory phenotype disrupts the cellular
510 asymmetry of homeostatic microglia and reduces the pool of non-centrosomal, parallel and mixed
511 oriented MTs, leading to their rearrangement into a radial array of uniformly oriented MTs
512 characteristic of the ameboid shape. In addition, while in pro-inflammatory microglia all the MTs
513 are anchored to a centrosomal region, homeostatic microglia nucleate acentrosomal MTs from
514 Golgi outposts located far from the cell body at the branching points of microglia ramifications,
515 resembling the structure of the dendritic tree of mature neurons (Horton *et al.*, 2005; Nguyen *et*
516 *al.*, 2014; Yau *et al.*, 2014) or the organization of oligodendrocytic myelin sheaths (Fu *et al.*, 2019;
517 Valenzuela *et al.*, 2020). This Golgi outpost-dependent non-centrosomal nucleation contrasts to
518 pro-inflammatory and anti-inflammatory microglia in which the Golgi apparatus displays a
519 compact perinuclear location (Li, Ahat and Wang, 2019), suggesting that in reactive microglia
520 cellular arborization is reduced by restricting the Golgi to a region adjacent to the centrosome,
521 which acts as the major MT nucleator in these cells. Indeed, we observed that the acquisition of a
522 pro-inflammatory phenotype is characterized by γ-tubulin redistribution to puncta located to a
523 pericentrosomal region, a feature we confirmed in retinal microglia residing in tissue. Co-
524 localization of γ-tubulin with pericentrin and anchoring of radial MTs to the puncta strongly
525 suggests that these protein assemblies are composed of PCM and act as pericentrosomal MTOCs.
526 Importantly, γ-tubulin redistribution during the transition to a pro-inflammatory phenotype did not
527 derive from centriolar duplication during cell division (Fuller *et al.*, 1995; Alvarado-Kristensson,
528 2018) as no more than 2 γ-tubulin^{+} puncta colocalized with centrin-3 in the same cell, an abundant

529 protein associated with the centrosome (Middendorp *et al.*, 2000). In addition, γ-tubulin
530 redistribution was strictly dependent on a dynamic MT cytoskeleton, suggesting that the increase
531 in MT dynamicity is necessary for the relocation of MT nucleating material to the centrosome.

532 We find that PCM maturation occurring in pro-inflammatory microglia negatively
533 regulates IL-1β release through a non-classical secretory pathway (Lacy and Stow, 2011). Indeed,
534 inhibition of PLK4 during the acquisition of a pro-inflammatory phenotype reduces
535 pericentrosomal γ-tubulin^{+} puncta formation, increases NLRP3 expression, and potentiates IL-
536 1β release without affecting the release of IL-6 and IL-10. NLRP3-inflammasome hyperactivation
537 is consistent with NLRP3 hyperactivation through NEK7 dephosphorylation by inhibition of
538 PLK4 in macrophages (Seoane *et al.*, 2020; Yang *et al.*, 2020). Given that the NLRP3-
539 inflammasome mediates interleukin activation (Hanisch, 2002), NLRP3-inflammasome
540 hyperactivation may account for the increase in IL-1β release and the accumulation of blebbing
541 microvesicles we observe in microglia stimulated *in vitro*. Interestingly, our results on cytokine
542 release upon PLK4-inhibition differ from those reported after long-term (7 days) inhibition in
543 macrophages activated with LPS (Vertii *et al.*, 2016)) suggesting that the response to loss of PLK4
544 activity is cell type specific or longer treatments may have either secondary or opposite effects.
545 Further studies are necessary to discriminate between these possibilities.

546 In summary, we identify a heretofore unique example of MT reorganization from a non-
547 centrosomal array of MTs with mixed polarity to a radial array in which all the MTs are uniformly
548 oriented and anchored either at the centrosome or pericentrosomal MTOCs. Our structural,
549 functional and in tissue analyses further demonstrate that acentrosomal MT nucleation at Golgi
550 outposts may play an important role in supporting the patrolling phenotype of microglia cells, that
551 tubulin remodeling enables microglia reactivity *in vitro* and in tissue, and that targeting PCM
552 maturation in reactive microglia may represent a new approach to limit tissue damage during
553 neurodegenerative disease in which microgliosis contributes to neuronal injury and cognitive
554 decline (Heneka, Kummer and Latz, 2014; Colonna and Butovsky, 2017).
555
556
557
558
559

560 **Star Methods**

561

562 **Key resources table**

REAGENT or RESOURCE	SOURCE	IDENTIFIERR
Antibodies		
Camsap2 (rabbit polyclonal)	Novus Biologicals	Cat# NBP1-26645; RRID AB_1852845
γ Tubulin (rabbit polyclonal)	Invitrogen	Cat# PA1-28042; RRID AB_2256789
γ Tubulin (mouse monoclonal)	Sigma-Aldrich	Cat# T5326; RRID AB_532292
Tyr Tubulin (rat monoclonal)	Millipore	Cat# MAB1864; RRID AB_2128189
Acetylated Tub (Mouse monoclonal)	Sigma-Aldrich	Cat# T7451; RRID AB_609894
α-Tubulin (mouse monoclonal)	Sigma-Aldrich	Cat# T6199; RRID AB_477583
De-tyr Tubulin (Rabbit polyclonal)	Millipore	Cat# AB3201; RRID AB_177350
EB1 (Mouse monoclonal)	BD Biosciences	Cat# 610535; RRID AB_397892
Pericentrin (Rabbit polyclonal)	Abcam	Cat# Ab4448; RRID AB_304461
Centrin3 (Mouse monoclonal)	Abnova	Cat# H00001070-M01; RRID AB_304461
GM130 (Mouse monoclonal)	BD Biosciences	Cat# 610822; RRID AB_398141
IBA1 (Rabbit polyclonal)	FujiFilm	Cat# 019-19741; RRID AB_839504
Atto488 Phalloidin	Sigma-Aldrich	Cat# 49409
Alexa Fluor 488 goat anti-mouse	Invitrogen	Cat# A11001; RRID AB_2534069
488 goat anti-rat	Invitrogen	Cat# A11006; RRID AB_141373
488 goat anti-rabbit	Invitrogen	Cat# A11008; RRID AB_143165
594 goat anti-mouse	Invitrogen	Cat# A11032; RRID AB_2534091

647 goat anti-rabbit	Invitrogen	Cat# A32733; RRID AB_2633282
CF 594 goat anti-rat	Sigma-Aldrich	Cat# SAB4600111
Chemicals, peptides, and recombinant proteins		
LPS from E.Coli O55:B5	Sigma-Aldrich	Cat# L5418
LPS from E.Coli O111:B4	Sigma-Aldrich	Cat# L4391
Murine recombinant IL-4	PEPROTECH	Cat# 214-14
Murine recombinant IFNγ	PEPROTECH	Cat# 315-05
Taxol	Sigma-Aldrich	Cat# PHL89806
Centrinone (PLK4 inhibitor)	Tocris	Cat# 5687
Nocodazole	Sigma-Aldrich	Cat# 31430-18-9
Hoechst	Sigma-Aldrich	Cat# 23491-45-4
Propidium Iodide	Sigma-Aldrich	Cat# 25535-16-4
Poly-L-lysine hydrobromide	Sigma-Aldrich	Cat# P6282
Hexamethyldisilazane	Sigma-Aldrich	Cat# 999-97-3
Dulbecco′s Modified Eagle′s Medium (DMEM)	Sigma-Aldrich	Cat# D6546
Fetal bovine serum (FBS)	Gibco	Cat# 11573397
Phosphate-Buffered Saline (PBS) tablets	Sigma-Aldrich	Cat# P4417
Saponin	Sigma-Aldrich	Cat# 47036-50G-F
Critical commercial assays		
Mouse IL-6 Elisa Kit	Invitrogen	Cat# BMS603-2
Mouse IL-10 Elisa Kit	Invitrogen	Cat# 88-7105-88
Mouse IL1β Elisa Kit	Invitrogen	Cat# 88-7013-86
Quick RNA MiniPrep	Zymo Research, Freiburg, DE	Cat# R1055
iScript Reverse Transcription Supermix	Bio-Rad, Hercules, CA, USA	Cat# 1708840
Sybr Green	Bio-Rad, Hercules, CA, USA	Cat# 172-5124
NuPAGE™ 4 to 12%, Bis-Tris, 1.0 mm, Mini Protein	Invitrogen	Cat# NP0321PK2
SiR-Tubulin Kit	Cytoskeleton	Cat# CY-SC002
Immun-Star Western Chemiluminescence Kit	Bio-Rad	Cat#170-5070
Deposited data		
Max Intensity RadialProfile	This paper	https://github.com/ggosti/maxIntensityRadialProfile
Experimental models: Organisms/strains		

Mouse: C57BL/6	Charles River Laboratories	027C57BL/6
Mouse: Cx3cr1$^{gfp/gfp}$	Jackson Laboratories	B6.129P2(Cg)-Cx3cr1tm1Litt/J bred with C57BL6/j
Oligonucleotides		
GAPDH forward: TCGTCCCGTAGACAAAATGG	Sigma-Aldrich	Custom
GAPDH reverse: TTGAGGTCAATGAAGGGGTC	Sigma-Aldrich	Custom
Ym1 forward: CAGGTCTGGCAATTCTTCTGAA	Sigma-Aldrich	Custom
Ym1 reverse: GTCTTGCTCATGTGTGTAAGTGA	Sigma-Aldrich	Custom
Fizz1 forward: CCAATCCAGCTAACTATCCCTCC	Sigma-Aldrich	Custom
Fizz1 reverse: ACCCAGTAGCAGTCATCCCA	Sigma-Aldrich	Custom
Tnfα forward: GTGGAACTGGCAGAAGAG	Sigma-Aldrich	Custom
Tnfα reverse: CCATAGAACTGATGAGAGG	Sigma-Aldrich	Custom
IL1β forward: GCAACTGTTCCTGAACTCAACT	Sigma-Aldrich	Custom
IL1β reverse: ATCTTTTGGGGTCCGTCAACT	Sigma-Aldrich	Custom
iNOS forward: ACATCGACCCGTCCACAGTAT	Sigma-Aldrich	Custom
iNOS reverse: CAGAGGGGTAGGCTTGTCTC	Sigma-Aldrich	Custom
Software and algorithms		
GraphPad Prism v9.0	GraphPad Software Inc.	https://www.graphpad.com
FIJI/ImageJ 1.53c	(Schindelin *et al.*, 2012)	http://www.imagej.nih.gov/ij
ImageJ 1.50i	Wayne Radband, National institute of Health, USA	http://imagej.nih.gov/ij
Metamorph 7.10.2	Molecular Devices	https://www.moleculardevices.com/
Imaris 8.1.2	Oxford Instruments	https://imaris.oxinst.com/
FlowJo v10.7.1	TreeStar, Ashland, OR, USA	https://www.flowjo.com/
Quantity One software	Biorad	https://www.bio-rad.com
NIS-elements	Nikon	https://www.microscope.healthcare.nikon.com/
Anaconda3	Anaconda Inc.	https://www.anaconda.com

Python 3.8.5	Python Software Foundation.	http://www.python.org
Numpy 1.19.2	(Harris *et al.*, 2020)	https://numpy.org
Matplotlib 3.3.2	(Hunter, 2007)	https://matplotlib.org
Scikit-image 0.17.2	(Van Der Walt *et al.*, 2014)	https://scikit-image.org
Other		
Killik O.C.T. Compound	Bio-Optica	Cat# 05-9801
µ-Slide 8 Well	Ibidi	Cat# 80826
ibidi Mounting Medium	Ibidi	Cat# 50001
ProLong Glass Antifade Mountant	Invitrogen	Cat# P36982
Superfrost ultra plus slides	Thermo Scientific	Cat# 10149870

METHOD DETAILS

Primary murine microglia culture and treatment

Primary cortical glial cells were prepared from 0- to 2-d-old mice as previously described (Rosito *et al.*, 2012). Briefly, cerebral cortices were chopped and digested in 30 U/ml papain for 40 min at 37 °C followed by gentle trituration. The dissociated cells were washed, suspended in Dulbecco′s Modified Eagle′s Medium (DMEM, Sigma-Aldrich) with 10% FBS (Gibco) and 2 mM L-glutamine and plated at a density of 9–10 x 10^5 in 175 cm^2 cell culture flasks. At confluence (10 – 12 DIV), glial cells were shaken for 2 h at 37 °C to detach and collect microglial cells. These procedures gave an almost pure (< 1% astrocyte contamination) microglial cell population. Microglia cells were plated at a density of $7x10^3/cm^2$ (to prevent cell contact activation) in astrocytes conditioned medium /DMEM 2,5% FBS (1:1). The day after plating microglia cells were treated for 48 h with IFNγ (20 ng/ml) and LPS (100 ng/ml) or with IL-4 (20 ng/ml) to obtain the pro-inflammatory or anti-inflammatory phenotype, respectively. To disassemble MTs, homeostatic microglia were treated with 2 µM nocodazole (Sigma-Aldrich) added to the culture medium for 1 h at 37 °C. Samples were then kept on ice and washed 5x times with ice-cold medium. MTs were allowed to regrow in conditioned medium without nocodazole for 15 min and 120 min at 37 °C. Right before fixation, free tubulin was rapidly extracted using a MT-preserving extraction buffer (60 mM PIPES, 25 mM HEPES, 10 mM EGTA, 2 mM $MgCl_2$, 0.1% saponin, pH 6.9, Zhu and Kaverina, 2011) for 20 sec at 37 °C. Cells were subsequently fixed with methanol at -20 °C for 4 min and processed for immunofluorescence staining. To stabilize MTs, microglia

584 cells were treated for 24 h with 1 nM and 5 nM Taxol (Sigma-Aldrich) alone or together with
585 IFNγ (20 ng/ml) and LPS (100 ng/ml). To inhibit PLK4, microglia cells were pre-treated with 125
586 nM Centrinone (Tocris) for 12 h prior to stimulation for 48 h with IFNγ (20 ng/ml) and LPS (100
587 ng/ml).
588
589 **Immunofluorescence staining on fixed cells**
590 Methanol fixation at -20 °C was elected for preserving an intact MT cytoskeleton: culture medium
591 was removed and cells were fixed with pre-cooled 100% methanol at -20°C for 4 min prior to re-
592 hydration with Phosphate-buffered saline (PBS, 0.01 M phosphate buffer, 0.0027 M potassium
593 chloride and 0.137 M sodium chloride, pH 7.4, at 25 °C, Sigma-Aldrich) for at least 30 min at RT
594 To preserve membrane associated components, cells were fixed with 4% paraformaldehyde
595 (PFA)/PBS for 15 min at RT and then washed with PBS. When PFA fixed, cells were
596 permeabilized with 0.1% Triton X-100/PBS for 1 to 3 min. After 2 washes in PBS, cells were
597 blocked with 3% bovine serum albumin (BSA, Sigma-Aldrich) in PBS for 1 h at RT Primary
598 antibodies (Rabbit Camsap1L1, Novus Biologicals, 1:200; rabbit γ-tubulin, Invitrogen, 1: 5000;
599 mouse γ tubulin, Sigma-Aldrich, 1:1000; rat Tyrosinated tubulin YL 1/2, Millipore, 1:1000; mouse
600 Acetylated tubulin clone 6-11B-1, Sigma-Aldrich, 1:1000; mouse α-tubulin clone DM1A, Sigma-
601 Aldrich, 1:500; rabbit Detyrosinated α-tubulin, Millipore, 1:1000; mouse EB1, BD Biosciences,
602 1:100; rabbit Pericentrin, Abcam, 1:1500; mouse Centrin3, Abnova, 1:100; mouse GM130, BD
603 Biosciences, 1:600; rabbit IBA-1, FujiFilm, 1:300; Atto 488 Phalloidin, Sigma-Aldrich, 1:50) were
604 incubated in 1.5% BSA in PBS for 2 h (RT) or overnight (+4°C). Cells were then extensively
605 washed and stained with fluorophore-conjugated secondary antibodies in PBS (Alexa Fluor 488
606 goat anti-mouse, 488 goat anti-rat, 488 goat anti-rabbit, 594 goat anti-mouse, 647 goat anti-rabbit,
607 Invitrogen; CF 594 goat anti-rat, Sigma-Aldrich; 1:500) and Hoechst (Sigma-Aldrich) for nuclei
608 visualization for 1 h at RT prior to wash and mounting using Ibidi Mounting Medium.
609
610 **MT dynamics assay**
611 For live fluorescence imaging to measure MT dynamics, cells were incubated with 100 nM SiR-
612 Tubulin (SpiroChrome) at 37 °C for 30 min and washed with conditioned medium prior to
613 visualization to improve signal to noise ratio. 10 μM Verapamil was added to inhibit efflux pumps
614 and improve labeling. Live wide-field fluorescence imaging of SiRTub-labeled MTs was

615 performed on a Olympus IX73 microscope, LDI laser source and CoolSNAP Myo camera, 4.54
616 µm pixels (Photometrics) with a built-in incubator, maintaining the temperature at 37 °C during
617 recordings. Acquisitions were performed for 4 min (1 frame/4 sec) with a UPLSXAPO100x/1.45
618 oil objective and then analyzed with ImageJ software (see *Image preparation and analysis*).
619
620 **Animals**
621 All procedures performed using laboratory animals were in accordance with the Italian and
622 European guidelines and were approved by the Italian Ministry of Health in accordance with the
623 guidelines on the ethical use of animals from the European Communities Council Directive of
624 September 20, 2010 (2010/63/UE). All efforts were made to minimize suffering and number of
625 animals used. Mice were housed in standard cages in a group of a maximum of 5 animals, with
626 light–dark cycles of 12 h at 22±2 °C. Wild type C57BL-6 male and pregnant mice were purchased
627 from Charles River and pups (P0-P2) were used to obtain primary glial cultures. Cx3cr1$^{gfp/gfp}$ male
628 mice were purchased from The Jackson Laboratory company (B6.129P2(Cg)-Cx3cr1tm1Litt/J);
629 the colony was established in our animal facility, and progenitors were bred to C57BL6J to obtain
630 cx3cr1$^{gfp/+}$ mice as we previously reported (Pagani et al., 2015).
631
632 **Intravitreal injection and EIU**
633 Adult C57BL6/J mice were intravitreally injected with sterile PBS (vehicle) or 5 ng/µl LPS from
634 *E. Coli* (O55:B5, Sigma Aldrich). Intravitreal injection of LPS has been previously reported as a
635 model of endotoxin induced uveitis (EIU) activating microglia in the retina (Becker *et al.*, 2001;
636 Rosenbaum *et al.*, 2011; Wang *et al.*, 2011; Chu *et al.*, 2016; Bell *et al.*, 2020). Animals were
637 anaesthetized with 100 mg/kg methadomidine and 0.25 mg/kg ketamine. Pupils were dilated using
638 1% tropicamide and 2.5% phenylephrine (Chauvin, Essex, UK) and a small guide hole was made
639 under the limbus with a 30G needle. The eye was gently massaged with a cotton swab to remove
640 a portion of the vitreous to avoid a post-injection reflux of vitreous and/or drug solution. Then, 1
641 µl of vehicle or LPS solution was intravitreally injected through the initial hole using a 34G
642 Hamilton syringe.
643
644 **Immunofluorescence staining on retinal tissue**

645 Cx3cr1$^{gfp/+}$ control mice were sacrificed at P70. CTRL (sham) and LPS intravitreally injected adult
646 C57BL6/J mice were sacrificed 20 h after the injection procedure.
647 Eyes were removed and kept in 4% PFA solution overnight. Eyes were then cryoprotected in 30%
648 sucrose and, after precipitation, frozen in isopentane prior to storage at -80 °C. Frozen eyes were
649 cut in 50-µm-thick sections with a Leica cryostat and processed for immunofluorescence staining
650 as published (Wu *et al.*, 2020). Briefly, slices were immersed for 30 min in a boiling 1 mM EDTA
651 solution (pH = 8.0) for antigen retrieval, then incubated with blocking solution (0.1% Triton X-
652 100, 3% BSA and 0.05% Tween-20 in PBS) for 1 h at RT. Sections were incubated with primary
653 antibodies (Iba1, FujiFilm, 1:500; γ-tubulin, clone GTU-88, Sigma-Aldrich, 1:500; GM130, BD
654 bioscience, 1:500) in diluted blocking solution overnight at 4 °C and 1 h at RT with fluorophore-
655 conjugated secondary antibodies (Alexa Fluor 488 goat anti-rabbit, 594 goat anti-mouse) and
656 Hoechst for nuclei visualization. The sections were mounted with anti-fade mounting medium
657 (Invitrogen).
658
659 **Confocal Spinning Disk and Structured Illumination (SIM) microscopy**
660 For fluorescence imaging of fixed samples, images were collected with spinning disk confocal
661 microscopy on a Nikon Eclipse Ti equipped with X-Light V2 spinning disk (CrestOptics),
662 combined with a VCS (Video Confocal Super resolution) module (CrestOptics) based on
663 structured illumination, and a LDI laser source (89 North) and Prime BSI Scientific CMOS
664 (sCMOS) camera, 6.5 µm pixels (Photometrics) or a CoolSNAP Myo camera, 4.54 µm pixels
665 (Photometrics), with a 10x/0.25 NA Plan E air objective, 40x/0.75 PlanApo l air objective, a
666 60x/1.4 PlanApo l oil objective and a 100x/1.45 Plan E oil objective. The used Z step size was 0.2
667 µm for spinning disk and 0.1 µm for VCS. In order to achieve super-resolution, raw data obtained
668 by the VCS module have been processed with a modified version of the joint Richardson-Lucy
669 (jRL) algorithm (Ingaramo *et al.*, 2014; Ströhl and Kaminski, 2015; Chakrova, Rieger and
670 Stallinga, 2016), where the out of focus contribution of the signal has been explicitly added in the
671 image formation model used in the jRL algorithm, and evaluated as a pixel-wise linear "scaled
672 subtraction" (Heintzmann and Benedetti, 2006) of the raw signal. Retinal sections images were
673 acquired on an Olympus IX73 microscope equipped with X-Light V3 spinning disk (CrestOptics),
674 LDI laser source and a Prime BSI Scientific CMOS (sCMOS), 6.5 µm pixels (Photometrics) with
675 a UPLSXAPO100x/1.45 oil objective. All the images were acquired by using Metamorph software

676 version 7.10.2. (Molecular Devices) and then analyzed with ImageJ software (see *Image*
677 *preparation and analysis*).
678
679 **Image preparation and analysis**
680 For image preparation, we used the open-source software ImageJ (Fiji project, Schindelin *et al.*,
681 2012) for adjustments of levels and contrast, maximum intensity projections, and thresholding
682 signals for fluorescence intensity analysis.
683 *Radial profile analysis.* For tyrosinated α-tubulin, CAMSAP2 and γ tubulin distribution analysis,
684 microglia cells were fixed in methanol at -20 °C for 4 min or PFA 4% for 15 min and then stained
685 with an anti-tyrosinated tubulin, CAMSAP2 or γ tubulin antibody according to the
686 immunofluorescence protocol, and Hoechst for nuclei visualization. Images obtained by confocal
687 microscopy were analyzed with ImageJ to identify the coordinates of the center of the nucleus in
688 each cell and to generate single-cell masks based on the morphology of each cell. A Python script
689 (see Supplementals) was written to apply an Otsu threshold to the images (Otsu, 1979) and to
690 perform a radial scanning of fluorescence values, starting from the center of the nucleus of each
691 cell, with a resolution of 0.065 µm. Maximum value radial profile was defined as the maximum
692 fluorescence intensity (a.u.) for each concentric circle with an increasing distance from the nucleus
693 center. For each analyzed microglia cell the radial profile of the maximum value of fluorescence
694 intensity (a.u.) was computed and plotted. Plots were smoothed with a resolution of 0.5 µm. All
695 data points were exported into a Microsoft Excel 2010 (Microsoft Corporation) compatible format.
696 In CAMSAP2 analysis, only cytoplasmic staining was analyzed. Curve fit was performed using a
697 single exponential decay function on GraphPad Prism 9.0 (Y=(Y0 - Plateau)*exp(-K*X) +
698 Plateau).
699 *MT dynamics analysis.* Analysis of MT dynamics was performed by tracing the lengths of the MTs
700 via the "freehand line" tracing tool in ImageJ. Changes in length between successive frames were
701 exported into an Excel sheet to determine the growth, shortening and pause events for each MT.
702 Only changes > 0.5 µm were considered growth or shortening events (Dhamodharan and
703 Wadsworth, 1995; Rusan *et al.*, 2001). MT dynamics parameters were defined as follows:
704 growth/shrinkage rate: distance (µm) covered in growth or shrinkage per second;%
705 pause/growth/shrinkage: number of frames in pause/growth/shrinkage divided total number of
706 frames X 100; catastrophe/rescue frequency (sec^{-1}): number of catastrophe or rescue events

707 divided by the product of the time of analysis and the percentage of growth or shrinkage; MT
708 dynamicity: the sum of total length in growth and shortening divided by the time of analysis.
709 *In vitro cell morphology analysis*. Cell morphology analysis was performed using a quantitative
710 measurement of cell area; cell solidity is expressed as the ratio between cell area and convex area.
711 Measurements were obtained with the Particle Analysis tool and images were processed with
712 ImageJ.
713 *Extracellular vesicle analysis*. For the statistical analysis of EV blebbing from the surface of
714 microglia, 20 microglia cells per sample, collected in four different areas of the support, were
715 randomly selected and scanned to count and measure the visualized vesicles. The ImageJ software
716 was used to count and measure the vesicle major axis.
717 *Immunofluorescence signal quantification.*
718 For immunofluorescence signal quantification, cells were selected on the basis of the
719 representative morphology: ramified for homeostatic, ameboid for pro-inflammatory and bipolar
720 for anti-inflammatory states. Detyr/Tyr tubulin ratio and Acetyl/Tyr tubulin ratio were calculated
721 from the mean gray values of the respective immunofluorescence signals, obtained from sum slices
722 z-projections of 15 confocal planes after background subtraction (calculated as mean gray value
723 of three circle background areas). EB1 anterograde or retrograde comets were defined from the
724 EB1 fluorescence signal gradient from single plane images, measured with the "plot profile" tool
725 of ImageJ. For Golgi stacks analysis, GM130 maximum intensity z-projection
726 immunofluorescence images were uniformly thresholded on ImageJ by setting the same minimum
727 values ('Default' threshold) to identify single Golgi stacks; a single Golgi stack was defined as a
728 non-round object (roundness < 0.9) with a major axis length > 0.5 μm. For GM130- γ-tubulin co-
729 staining analysis, GM130 and tubulin signals from max intensity z-projections were uniformly
730 processed among different images increasing the 'brightness' and 'contrast' parameters by the
731 same percentage. γ-tubulin signal over cell area was calculated as percentage of cell area covered
732 by γ tubulin signal; γ-tubulin signal threshold was uniformly applied on MetaMorph analysis
733 software by setting the same minimum values to all images.
734 Two or more distinct γ-tubulin^{+} puncta were identified by counting the peaks of fluorescence
735 intensity on a linescan drawn through the centroid of each puncta using the free-hand tool on
736 ImageJ; The Find Peaks ImageJ plugin was used to identify the peaks by setting the minimum
737 peak amplitude value at 100 grey values. Puncta were identified in a 132x132 pixels pericentriolar

738 region after uniformly thresholding max intensity z-projections ('Default' threshold); integrated
739 density was calculated in ImageJ as mean gray value*thresholded area. Pericentrin and Centrin-3-
740 γ-tubulin co-localization analysis was performed by defining Pericentrin and Centrin-3^+ puncta as
741 described above for γ-$tubulin^+$ puncta.
742 *Retinal microglia cell skeleton analysis.* Morphology of microglia cells in retinal sections was
743 analyzed on max intensity z-projections; only entirely visible cells inside the acquisition field were
744 analyzed; cells were isolated and then skeletonized on binary images, using the dedicated ImageJ
745 plug-in; branches, endpoints and junction number was calculated from the skeletonized image.
746
747 **Real time PCR**
748 RNA was extracted from microglia cells with the Quick RNA MiniPrep (Zymo Research,
749 Freiburg, DE) and retrotranscribed with iScript Reverse Transcription Supermix for Real-time
750 PCR (RT-PCR) (Bio-Rad, Hercules, CA, USA). RT-PCR was carried out using Sybr Green
751 (Biorad) according to the manufacturer's instructions. The PCR protocol consisted of 40 cycles of
752 denaturation at 95 °C for 30 s and annealing/extension at 60 °C for 30 s. For quantification, the
753 comparative Threshold Cycle (Ct) method was used. The Ct values from each gene were
754 normalized to the Ct value of GAPDH in the same RNA samples. Relative quantification was
755 performed using the $2^{-\Delta\Delta Ct}$ method (Schmittgen and Livak, 2008) and expressed as fold change in
756 arbitrary values. Primer sequences are listed in table S1.
757
758 **SEM analysis**
759 Samples were fixed in a solution of 1.5% Glutaraldehyde in 0.1 M Cacodylate buffer for 2 h at RT
760 and post-fixed in 1% osmium tetroxide in Milli q (MQ) H_2O for 2 h. After several washes in MQ
761 H_2O, the samples were subsequently dehydrated in rising concentrations of ethanol in H_2O
762 solutions (from 30% to 100%), 1:1 ethanol:hexamethyldisilazane (HMDS, Sigma-Aldrich) and
763 100% HMDS and dried overnight in air. Finally, the samples were sputtered with a 10 nm gold
764 layer and analyzed using a JEOL JSM-6490LA Scanning Electron Microscope (SEM) operating
765 at 10 KV of accelerating voltage.
766
767 **Western blot**

768 Cells were lysed in Laemmli sample buffer and boiled at 95 °C for 5 min. Proteins were separated
769 by 4-12% Bis-Tris gel (Invitrogen) and transferred onto nitrocellulose membrane. After blocking
770 in 5% milk/TBS (Tris 20 mM, NaCl 150 mM), membranes were incubated with primary antibodies
771 at 4 °C overnight prior to 1 h incubation with secondary antibodies and signal detected using a
772 commercial chemiluminescent assay (Immun-Star WesternC Kit; Bio-Rad). Image acquisition was
773 performed with ChemiDoc MP imaging system (Bio-Rad) and densitometric analysis was
774 performed with Quantity One software (Biorad).
775
776 **Cell cycle assay**
777 Microglia cells were collected by following trypsin treatment. Cells were rinsed twice with
778 phosphate buffered saline (PBS pH 7.4) and collected by centrifugation. Pellets were resuspended
779 in ice cold 70% ethanol and stored at 4 °C for 1 h. Cells were collected by centrifugation, rinsed
780 twice in PBS and resuspended in 20 µg/ml propidium iodide (PI) in PBS with 50 µg/ml RNase A
781 for a minimum of 30 min. After PI incubation, Flow cytometry analysis of DNA content was
782 performed as reported and analyzed using a BD LSRFortessa (BD Biosciences, San Jose, CA,
783 USA). The percentage of cells in different phases of the cell cycle was determined using the
784 FlowJo V10.7.1 computer software (TreeStar, Ashland, OR, USA). At least 10.000 events for each
785 sample were acquired.
786
787 **Statistical analysis**
788 The n number for each experiment and details of statistical analyses are described in the figure
789 legends or main text. Data are reported as mean ± SEM; when not normally distributed, data are
790 reported as median ± interquartile range. Origin 6 and GraphPad Prism 9 software were used for
791 statistical analysis. Normality tests were performed with Prism 9 and nonparametric tests were
792 used when appropriate. Significant differences are indicated in the figures by * $p < 0.05$, ** $p <$
793 0.01, *** $p < 0.001$. Notable non-significant differences are indicated in the figures by ns.
794
795 **Supplementary material**
796 Movie S1. Time-lapse acquisition of SiR-Tubulin labeled MTs in homeostatic microglia, Related
797 to Figure 1

798 Movie S2. Time-lapse acquisition of SiR-Tubulin labeled MTs in pro-inflammatory microglia,
799 Related to Figure 1
800 Movie S3. Time-lapse acquisition of SiR-Tubulin labeled MTs in anti-inflammatory microglia,
801 Related to Figure 1
802 Table 1. MT dynamicity parameters in homeostatic and activated microglia, Related to Figure 1
803 Figure S1. Molecular and morphological characterization of homeostatic, pro-inflammatory and
804 anti-inflammatory primary microglia, Related to Figure 1
805 Figure S2. Analysis of EB1 and CAMSAP2 expression in homeostatic, pro-inflammatory and anti-
806 inflammatory microglia, Related to Figure 2
807 Figure S3. Molecular, morphological and functional characterization of microglia non-
808 centrosomal MTs nucleation in primary cultures and in retinal slices, Related to Figure 3
809 Fig S4. Analysis of pericentriolar material maturation during microglia pro-inflammatory
810 activation, Related to Figure 4
811 Fig S5. Characterization of in vivo microglia activation in the LPS-induced uveitis model, Related
812 to Figure 4
813

814 **Acknowledgements**

815 This study was supported by NIH/NIA R56AG050658 and NIH/NINDS R21 NS120076-01 grants
816 to F.B. and a Fulbright Award to F.B. and S.D.A. This research was also funded by the
817 CrestOptics-IIT JointLab for Advanced Microscopy (to S.D.A. and G.C.R.); the Regione Lazio
818 MARBEL Life2020 and Bio3DBrain FSE 2014-2020 grants (to S.D.A); by Sapienza University
819 RM118163E0297F84 and PH12017270934C3C grants (to S.D.A.) and Fondazione Istituto
820 Italiano di Tecnologia (to M.R. and C.S.). C.S. was also supported by the Ph.D. program in Life
821 Science at Sapienza University in Rome. The research leading to these results has been also
822 supported by European Research Council Synergy grant ASTRA (n. 855923 to G.C.R.). The
823 authors wish to the Animal Facility of Physiology and Pharmacology Department of Sapienza
824 University. Graphical abstract was created using BioRender.com. We are grateful to David Sulzer
825 for comments on the manuscript and useful discussions.
826

827 **Author Contributions**

F.B., S.D.A., and M.R. designed the study and wrote the manuscript. C.S, M.R., M.M., D.D., F.C., G.P., M.G. and A.I. performed experiments and generated primary data. G.G. generated code; C.S., M.R., F.C., D.D., G.P. M.M., M.G. and S.D.A. performed data analysis. E.D.L., S.D.P., G.C.R, D.R., and R.G. provided helpful insights and contributed key techniques. F.B. and S.D.A supervised data analysis and experiments.

Materials availability

This study did not generate new unique reagents. The data that support the findings of this study are available from the corresponding author upon reasonable request. The code is available at https://github.com/ggosti/maxIntensityRadialProfile.

Additional information

The authors declare no competing financial interest.

References

Akhmanova, A. and Hoogenraad, C. C. (2015) 'Microtubule minus-end-targeting proteins', *Current Biology*. Elsevier Ltd, 25(4), pp. R162–R171. doi: 10.1016/j.cub.2014.12.027.

Akhmanova, A. and Steinmetz, M. O. (2019) 'Microtubule minus-end regulation at a glance', *Journal of cell science*, 132(11), pp. 1–7. doi: 10.1242/jcs.227850.

Alieva, I. B. *et al.* (2015) 'Centrosome nucleates numerous ephemeral microtubules and only few of them participate in the radial array', *Cell Biology International*, 39(11), pp. 1203–1216. doi: 10.1002/cbin.10492.

Alvarado-Kristensson, M. (2018) 'Γ-Tubulin As a Signal-Transducing Molecule and Meshwork With Therapeutic Potential', *Signal Transduction and Targeted Therapy*. Springer US, 3(1), pp. 1–6. doi: 10.1038/s41392-018-0021-x.

Baas, P. W. *et al.* (1988) 'Polarity orientation of microtubules in hippocampal neurons: Uniformity in the axon and nonuniformity in the dendrite', *Proceedings of the National Academy of Sciences of the United States of America*, 85(21), pp. 8335–8339. doi: 10.1073/pnas.85.21.8335.

Baas, P. W. *et al.* (1991) 'Microtubule dynamics in axons and dendrites', *Journal of Neuroscience Research*, 30(1), pp. 134–153. doi: 10.1002/jnr.490300115.

Baas, P. W. *et al.* (2016) 'Stability properties of neuronal microtubules', *Cytoskeleton*, 73(9), pp.

859 442–460. doi: 10.1002/cm.21286.
860 Bambo, M. P. *et al.* (2015) 'Visual function and retinal nerve fibre layer degeneration in patients
861 with Alzheimer disease: correlations with severity of dementia', *Acta Ophthalmologica*, 93(6), pp.
862 e507–e508. doi: 10.1111/aos.12635.
863 Bartolini, F. and Gundersen, G. G. (2006) 'Generation of noncentrosomal microtubule arrays',
864 *Journal of Cell Science*, 119(20), pp. 4155–4163. doi: 10.1242/jcs.03227.
865 Basilico, B. *et al.* (2019) 'Microglia shape presynaptic properties at developing glutamatergic
866 synapses', *Glia*, 67(1), pp. 53–67. doi: 10.1002/glia.23508.
867 Basilico, B. *et al.* (2021) 'Microglia control glutamatergic synapses in the adult mouse
868 hippocampus', *Glia*, (September), pp. 1–23. doi: 10.1002/glia.24101.
869 Becker, M. D. *et al.* (2001) 'Inhibition of leukocyte sticking and infiltration, but not rolling, by
870 antibodies to ICAM-1 and LFA-1 in murine endotoxin-induced uveitis', *Investigative*
871 *Ophthalmology and Visual Science*, 42(11), pp. 2563–2566.
872 Bell, O. H. *et al.* (2020) 'Single Eye mRNA-Seq Reveals Normalisation of the Retinal Microglial
873 Transcriptome Following Acute Inflammation', *Frontiers in Immunology*, 10(January). doi:
874 10.3389/fimmu.2019.03033.
875 Bernier, L. P. *et al.* (2019) 'Nanoscale Surveillance of the Brain by Microglia via cAMP-Regulated
876 Filopodia', *Cell Reports*. ElsevierCompany., 27(10), pp. 2895-2908.e4. doi:
877 10.1016/j.celrep.2019.05.010.
878 Bohlen, C. J. *et al.* (2017) 'Diverse Requirements for Microglial Survival, Specification, and
879 Function Revealed by Defined-Medium Cultures', *Neuron*. Elsevier Inc., 94(4), pp. 759-773.e8.
880 doi: 10.1016/j.neuron.2017.04.043.
881 Bolasco, G. *et al.* (2018) 'Three-dimensional nanostructure of an intact microglia cell', *Frontiers*
882 *in Neuroanatomy*, 12(December), pp. 1–5. doi: 10.3389/fnana.2018.00105.
883 Burton, P. R. and Paige, J. L. (1981) 'Polarity of axoplasmic microtubules in the olfactory nerve
884 of the frog.', *Proceedings of the National Academy of Sciences*, 78(5), pp. 3269–3273. doi:
885 10.1073/pnas.78.5.3269.
886 Chakrova, N., Rieger, B. and Stallinga, S. (2016) 'Deconvolution methods for structured
887 illumination microscopy', *Journal of the Optical Society of America A*, 33(7), p. B12. doi:
888 10.1364/josaa.33.000b12.
889 Chang, L. Y. L. *et al.* (2014) 'Alzheimer's disease in the human eye. Clinical tests that identify

890 ocular and visual information processing deficit as biomarkers', *Alzheimer's and Dementia*, 10(2),
891 pp. 251–261. doi: 10.1016/j.jalz.2013.06.004.
892 Chu, C. J. *et al.* (2016) 'Multimodal analysis of ocular inflammation using the endotoxin-induced
893 uveitis mouse model', *DMM Disease Models and Mechanisms*, 9(4), pp. 473–481. doi:
894 10.1242/dmm.022475.
895 Colonna, M. and Butovsky, O. (2017) 'Microglia function in the central nervous system during
896 health and neurodegeneration', *Annual Review of Immunology*, 35, pp. 441–468. doi:
897 10.1146/annurev-immunol-051116-052358.
898 Cordella, F. *et al.* (2021) 'Antibiotics Treatment Modulates Microglia–Synapses Interaction',
899 *Cells*, 10(10), p. 2648. doi: 10.3390/cells10102648.
900 Davalos, D. *et al.* (2005) 'ATP mediates rapid microglial response to local brain injury in vivo',
901 *Nature Neuroscience*, 8(6), pp. 752–758. doi: 10.1038/nn1472.
902 Davis, B. K., Wen, H. and Ting, J. P.-Y. (2011) 'The Inflammasome NLRs in Immunity,
903 Inflammation, and Associated Diseases', *Annual Review of Immunology*, 29(1), pp. 707–735. doi:
904 10.1146/annurev-immunol-031210-101405.
905 Dhamodharan, R. and Wadsworth, P. (1995) 'Modulation of microtubule dynamic instability in
906 vivo by brain microtubule associated proteins', *Journal of Cell Science*, 108(4), pp. 1679–1689.
907 doi: 10.1242/jcs.108.4.1679.
908 Durafourt, B. A. *et al.* (2012) 'Comparison of polarization properties of human adult microglia
909 and blood-derived macrophages', *Glia*, 60(5), pp. 717–727. doi: 10.1002/glia.22298.
910 Etienne-Manneville, S. (2013) 'Microtubules in cell migration', *Annual Review of Cell and*
911 *Developmental Biology*, 29, pp. 471–499. doi: 10.1146/annurev-cellbio-101011-155711.
912 Fu, M. meng *et al.* (2019) 'The Golgi Outpost Protein TPPP Nucleates Microtubules and Is Critical
913 for Myelination', *Cell*. Elsevier Inc., 179(1), pp. 132-146.e14. doi: 10.1016/j.cell.2019.08.025.
914 Fuller, S. D. *et al.* (1995) 'The core of the mammalian centriole contains γ-tubulin', *Current*
915 *Biology*, 5(12), pp. 1384–1393. doi: 10.1016/S0960-9822(95)00276-4.
916 Gadadhar, S. *et al.* (2017) 'The tubulin code at a glance', *Journal of Cell Science*, 130(8), pp. 1347
917 LP – 1353. doi: 10.1242/jcs.199471.
918 Gordon, S. and Taylor, P. R. (2005) 'Monocyte and macrophage heterogeneity', *Nature Reviews*
919 *Immunology*, 5(12), pp. 953–964. doi: 10.1038/nri1733.
920 Grimaldi, A. *et al.* (2018) 'Inflammation, neurodegeneration and protein aggregation in the retina

921 as ocular biomarkers for Alzheimer's disease in the 3xTg-AD mouse model', *Cell Death and*
922 *Disease*. Springer US, 9(6). doi: 10.1038/s41419-018-0740-5.
923 Gustin, A. *et al.* (2015) 'NLRP3 inflammasome is expressed and functional in mouse brain
924 microglia but not in astrocytes', *PLoS ONE*, 10(6), pp. 1–19. doi: 10.1371/journal.pone.0130624.
925 Hanisch, U. K. (2002) 'Microglia as a source and target of cytokines', *Glia*, 40(2), pp. 140–155.
926 doi: 10.1002/glia.10161.
927 Hanslik, K. L. and Ulland, T. K. (2020) 'The Role of Microglia and the Nlrp3 Inflammasome in
928 Alzheimer's Disease', *Frontiers in Neurology*, 11(September), pp. 1–9. doi:
929 10.3389/fneur.2020.570711.
930 Harris, C. R. *et al.* (2020) 'Array programming with NumPy', *Nature*. Springer US, 585(7825),
931 pp. 357–362. doi: 10.1038/s41586-020-2649-2.
932 Heidemann, S. R., Landers, J. M. and Hamborg, M. A. (1981) 'Polarity orientation of axonal
933 microtubules', *Journal of Cell Biology*, 91(3 I), pp. 661–665. doi: 10.1083/jcb.91.3.661.
934 Heintzmann, R. and Benedetti, P. A. (2006) 'High-resolution image reconstruction in fluorescence
935 microscopy with patterned excitation', *Applied Optics*, 45(20), pp. 5037–5045. doi:
936 10.1364/AO.45.005037.
937 Heneka, M. T., Kummer, M. P. and Latz, E. (2014) 'Innate immune activation in
938 neurodegenerative disease', *Nature Reviews Immunology*. Nature Publishing Group, 14(7), pp.
939 463–477. doi: 10.1038/nri3705.
940 Herr, D. R. *et al.* (2020) 'Ultrastructural Characteristics of DHA-Induced Pyroptosis',
941 *NeuroMolecular Medicine*. Springer US, 22(2), pp. 293–303. doi: 10.1007/s12017-019-08586-y.
942 Horton, A. C. *et al.* (2005) 'Polarized secretory trafficking directs cargo for asymmetric dendrite
943 growth and morphogenesis', *Neuron*, 48(5), pp. 757–771. doi: 10.1016/j.neuron.2005.11.005.
944 Hunter, J. D. (2007) 'Matplotlib: A 2D Graphics Environment', *Computing in Science &*
945 *Engineering*, 9(3), pp. 90–95. doi: 10.1109/MCSE.2007.55.
946 Ilschner, S. and Brandt, R. (1996) 'The transition of microglia to a ramified phenotype is associated
947 with the formation of stable acetylated and detyrosinated microtubules', *Glia*, 18(2), pp. 129–140.
948 doi: 10.1002/(SICI)1098-1136(199610)18:2<129::AID-GLIA5>3.0.CO;2-W.
949 Ingaramo, M. *et al.* (2014) 'Richardson-Lucy deconvolution as a general tool for combining
950 images with complementary strengths', *ChemPhysChem*, 15(4), pp. 794–800. doi:
951 10.1002/cphc.201300831.

952 Janke, C. and Bulinski, J. C. (2011) 'Post-translational regulation of the microtubule cytoskeleton:
953 Mechanisms and functions', *Nature Reviews Molecular Cell Biology*, 12(12), pp. 773–786. doi:
954 10.1038/nrm3227.
955 Janke, C. and Magiera, M. M. (2020) 'The tubulin code and its role in controlling microtubule
956 properties and functions', *Nature Reviews Molecular Cell Biology*. Springer US, 21(6), pp. 307–
957 326. doi: 10.1038/s41580-020-0214-3.
958 Javaid, F. Z. *et al.* (2016) 'Visual and ocular manifestations of Alzheimer's disease and their use
959 as biomarkers for diagnosis and progression', *Frontiers in Neurology*, 7(APR). doi:
960 10.3389/fneur.2016.00055.
961 Ji, X. *et al.* (2021) 'NIMA-related kinase 7 amplifies NLRP3 inflammasome pro-inflammatory
962 signaling in microglia/macrophages and mice models of spinal cord injury', *Experimental Cell*
963 *Research*, 398(2), pp. 14–22. doi: 10.1016/j.yexcr.2020.112418.
964 Jiang, K. *et al.* (2014) 'Microtubule Minus-End Stabilization by Polymerization-Driven CAMSAP
965 Deposition', *Developmental Cell*. Elsevier Inc., 28(3), pp. 295–309. doi:
966 10.1016/j.devcel.2014.01.001.
967 Kavcic, V., Vaughn, W. and Duffy, C. J. (2011) 'Distinct visual motion processing impairments
968 in aging and Alzheimer's disease', *Vision Research*. Elsevier Ltd, 51(3), pp. 386–395. doi:
969 10.1016/j.visres.2010.12.004.
970 Kettenmann, H. *et al.* (2011) 'Physiology of Microglia', *Physiological Reviews*, 91(2), pp. 461–
971 553. doi: 10.1152/physrev.00011.2010.
972 Klinman, E. and Holzbaur, E. L. F. (2018) 'Walking Forward with Kinesin', *Trends in*
973 *Neurosciences*. Elsevier Ltd, 41(9), pp. 555–556. doi: 10.1016/j.tins.2018.07.006.
974 Lacy, P. and Stow, J. L. (2011) 'Cytokine release from innate immune cells: Association with
975 diverse membrane trafficking pathways', *Blood*, 118(1), pp. 9–18. doi: 10.1182/blood-2010-08-
976 265892.
977 Latz, E., Xiao, T. S. and Stutz, A. (2013) 'Activation and regulation of the inflammasomes', *Nature*
978 *Reviews Immunology*, 13(6), pp. 397–411. doi: 10.1038/nri3452.
979 Lee, D. H. *et al.* (2014) 'Neuromyelitis optica presenting with relapses under treatment with
980 natalizumab: A case report', *Journal of Medical Case Reports*, 8(1), pp. 2–4. doi: 10.1186/1752-
981 1947-8-155.
982 Li, J., Ahat, E. and Wang, Y. (2019) *Golgi structure and function in health, stress, and diseases*,

983 *Results and Problems in Cell Differentiation*. doi: 10.1007/978-3-030-23173-6_19.
984 Li, L. and Yang, X. J. (2015) 'Tubulin acetylation: Responsible enzymes, biological functions and
985 human diseases', *Cellular and Molecular Life Sciences*. Springer Basel, 72(22), pp. 4237–4255.
986 doi: 10.1007/s00018-015-2000-5.
987 Li, R. and Gundersen, G. G. (2008) 'Beyond polymer polarity: How the cytoskeleton builds a
988 polarized cell', *Nature Reviews Molecular Cell Biology*, 9(11), pp. 860–873. doi:
989 10.1038/nrm2522.
990 Lukinavičius, G. *et al.* (2014) 'Fluorogenic probes for live-cell imaging of the cytoskeleton',
991 *Nature Methods*, 11(7), pp. 731–733. doi: 10.1038/nmeth.2972.
992 Madry, C. *et al.* (2018) 'Microglial Ramification, Surveillance, and Interleukin-1β Release Are
993 Regulated by the Two-Pore Domain K+ Channel THIK-1', *Neuron*, 97(2), pp. 299-312.e6. doi:
994 10.1016/j.neuron.2017.12.002.
995 Martin, M. *et al.* (2018) 'Control of endothelial cell polarity and sprouting angiogenesis by
996 noncentrosomal microtubules', *eLife*, 7, pp. 1–37. doi: 10.7554/eLife.33864.
997 Meiring, J. C. M. and Akhmanova, A. (2020) 'Microtubules keep large cells in shape', *Journal of*
998 *Cell Biology*, 219(6), pp. 1–3. doi: 10.1083/JCB.202004031.
999 Middendorp, S. *et al.* (2000) 'A role for centrin 3 in centrosome reproduction', *Journal of Cell*
1000 *Biology*, 148(3), pp. 405–415. doi: 10.1083/jcb.148.3.405.
1001 Mitchison, T. and Kirschner, M. (1984) 'Dynamic instability of microtubule growth', *Nature*,
1002 312(5991), pp. 237–242. doi: 10.1038/312237a0.
1003 Nguyen, M. M. *et al.* (2014) 'γ-tubulin controls neuronal microtubule polarity independently of
1004 Golgi outposts', *Molecular Biology of the Cell*, 25(13), pp. 2039–2050. doi: 10.1091/mbc.E13-09-
1005 0515.
1006 Nimmerjahn, A., Kirchhoff, F. and Helmchen, F. (2005) 'Resting microglial cells are highly
1007 dynamic surveillants of brain parenchyma in vivo', *Neuroforum*, 11(3), pp. 95–96. doi:
1008 10.1515/nf-2005-0304.
1009 Nogales, E. *et al.* (1999) 'High-resolution model of the microtubule', *Cell*, 96(1), pp. 79–88. doi:
1010 10.1016/S0092-8674(00)80961-7.
1011 Ori-McKenney, K. M., Jan, L. Y. and Jan, Y. N. (2012) 'Golgi Outposts Shape Dendrite
1012 Morphology by Functioning as Sites of Acentrosomal Microtubule Nucleation in Neurons',
1013 *Neuron*. Elsevier Inc., 76(5), pp. 921–930. doi: 10.1016/j.neuron.2012.10.008.

1014 Otsu, N. (1979) 'A Threshold Selection Method from Gray-Level Histograms', *IEEE Transactions*
1015 *on Systems, Man, and Cybernetics*, 9(1), pp. 62–66. doi: 10.1109/TSMC.1979.4310076.
1016 Paolicelli, R. C. *et al.* (2011) 'Synaptic pruning by microglia is necessary for normal brain
1017 development', *Science*, 333(6048), pp. 1456–1458. doi: 10.1126/science.1202529.
1018 Parkhurst, C. N. *et al.* (2013) 'Microglia promote learning-dependent synapse formation through
1019 brain-derived neurotrophic factor', *Cell*. Elsevier Inc., 155(7), pp. 1596–1609. doi:
1020 10.1016/j.cell.2013.11.030.
1021 Perry, V. H., Nicoll, J. A. R. and Holmes, C. (2010) 'Microglia in neurodegenerative disease',
1022 *Nature Reviews Neurology*. Nature Publishing Group, 6(4), pp. 193–201. doi:
1023 10.1038/nrneurol.2010.17.
1024 Reck-Peterson, S. L. *et al.* (2018) 'The cytoplasmic dynein transport machinery and its many
1025 cargoes', *Nature Reviews Molecular Cell Biology*. Springer US, 19(6), pp. 382–398. doi:
1026 10.1038/s41580-018-0004-3.
1027 Rosenbaum, J. T. *et al.* (2011) 'Contrasting Ocular Effects of Local versus Systemic Endotoxin',
1028 *Investigative Ophthalmology and Visual Science*, 52(9), pp. 6472–6477. doi: 10.1167/iovs.11-
1029 7742.
1030 Rosito, M. *et al.* (2012) 'CXCL16 orchestrates adenosine A 3 receptor and MCP-1/CCL2 activity
1031 to protect neurons from excitotoxic cell death in the CNS', *Journal of Neuroscience*, 32(9), pp.
1032 3154–3163. doi: 10.1523/JNEUROSCI.4046-11.2012.
1033 Rusan, N. M. *et al.* (2001) 'Cell cycle-dependent changes in microtubule dynamics in living cells
1034 expressing green fluorescent protein-α tubulin', *Molecular Biology of the Cell*, 12(4), pp. 971–
1035 980. doi: 10.1091/mbc.12.4.971.
1036 Schindelin, J. *et al.* (2012) 'Fiji: An open-source platform for biological-image analysis', *Nature*
1037 *Methods*, 9(7), pp. 676–682. doi: 10.1038/nmeth.2019.
1038 Schmittgen, T. D. and Livak, K. J. (2008) 'Analyzing real-time PCR data by the comparative CT
1039 method', *Nature Protocols*, 3(6), pp. 1101–1108. doi: 10.1038/nprot.2008.73.
1040 Schroder, K. and Tschopp, J. (2010) 'The Inflammasomes', *Cell*, 140(6), pp. 821–832. doi:
1041 10.1016/j.cell.2010.01.040.
1042 Seoane, P. I. *et al.* (2020) 'The NLRP3-inflammasome as a sensor of organelle dysfunction', *The*
1043 *Journal of cell biology*, 219(12), pp. 1–12. doi: 10.1083/jcb.202006194.
1044 Sernagor, E., Eglen, S. J. and Wong, R. O. L. (2001) 'Development of retinal ganglion cell

1045 structure and function', *Progress in Retinal and Eye Research*, 20(2), pp. 139–174. doi:
1046 10.1016/S1350-9462(00)00024-0.
1047 Ströhl, F. and Kaminski, C. F. (2015) 'A joint Richardson-Lucy deconvolution algorithm for the
1048 reconstruction of multifocal structured illumination microscopy data', *Methods and Applications*
1049 *in Fluorescence*. IOP Publishing, 3(1), p. 14002. doi: 10.1088/2050-6120/3/1/014002.
1050 Tanaka, N. *et al.* (2012) 'Nezha/CAMSAP3 and CAMSAP2 cooperate in epithelial-specific
1051 organization of noncentrosomal microtubules', *Proceedings of the National Academy of Sciences*
1052 *of the United States of America*, 109(49), pp. 20029–20034. doi: 10.1073/pnas.1218017109.
1053 Valenzuela, A. *et al.* (2020) 'Golgi Outposts Nucleate Microtubules in Cells with Specialized
1054 Shapes', *Trends in Cell Biology*. Elsevier Ltd, 30(10), pp. 792–804. doi:
1055 10.1016/j.tcb.2020.07.004.
1056 Vertii, A. *et al.* (2016) 'The Centrosome Undergoes Plk1-Independent Interphase Maturation
1057 during Inflammation and Mediates Cytokine Release', *Developmental Cell*. Elsevier Inc., 37(4),
1058 pp. 377–386. doi: 10.1016/j.devcel.2016.04.023.
1059 Vinogradova, T., Miller, P. M. and Kaverina, I. (2009) 'Microtubule network asymmetry in motile
1060 cells: Role of Golgi-derived array', *Cell Cycle*, 8(14), pp. 2168–2174. doi: 10.4161/cc.8.14.9074.
1061 Van Der Walt, S. *et al.* (2014) 'Scikit-image: Image processing in python', *PeerJ*, 2014(1), pp. 1–
1062 18. doi: 10.7717/peerj.453.
1063 Wang, M. *et al.* (2011) 'Adaptive Müller cell responses to microglial activation mediate
1064 neuroprotection and coordinate inflammation in the retina', *Journal of Neuroinflammation*.
1065 BioMed Central Ltd, 8(1), p. 173. doi: 10.1186/1742-2094-8-173.
1066 Webster, D. R. and Borisy, G. G. (1989) 'Microtubules are acetylated in domains that turn over
1067 slowly.', *Journal of cell science*, 92 (Pt 1), pp. 57–65. doi: 10.1242/jcs.92.1.57.
1068 Wu, J. and Akhmanova, A. (2017) 'Microtubule-Organizing Centers', *Annual Review of Cell and*
1069 *Developmental Biology*, 33(1), pp. 51–75. doi: 10.1146/annurev-cellbio-100616-060615.
1070 Wu, Y. *et al.* (2020) 'The molecular chaperone Hsp90α deficiency causes retinal degeneration by
1071 disrupting Golgi organization and vesicle transportation in photoreceptors', *Journal of Molecular*
1072 *Cell Biology*, 12(3), pp. 216–229. doi: 10.1093/jmcb/mjz048.
1073 Yang, X. *et al.* (2020) ' PLK 4 deubiquitination by Spata2-CYLD suppresses NEK7-mediated
1074 NLRP3 inflammasome activation at the centrosome ', *The EMBO Journal*, 39(2), pp. 1–16. doi:
1075 10.15252/embj.2019102201.

1076 Yau, K. W. *et al.* (2014) 'Microtubule minus-end binding protein CAMSAP2 controls axon
1077 specification and dendrite development', *Neuron*, 82(5), pp. 1058–1073. doi:
1078 10.1016/j.neuron.2014.04.019.
1079 Yu, Z. *et al.* (2018) 'Epothilone B Benefits Nigral Dopaminergic Neurons by Attenuating
1080 Microglia Activation in the 6-Hydroxydopamine Lesion Mouse Model of Parkinson's Disease',
1081 *Frontiers in Cellular Neuroscience*, 12(September), pp. 1–13. doi: 10.3389/fncel.2018.00324.
1082 Zhu, X. and Kaverina, I. (2011) 'Quantification of asymmetric microtubule nucleation at
1083 subcellular structures', *Methods in Molecular Biology*, 777, pp. 235–244. doi: 10.1007/978-1-
1084 61779-252-6_17.
1085 Zimmerman, W. C. *et al.* (2004) 'Mitosis-specific Anchoring of γ Tubulin Complexes by
1086 Pericentrin Controls Spindle Organization and Mitotic Entry', *Molecular Biology of the Cell*,
1087 15(8), pp. 3642–3657. doi: 10.1091/mbc.e03-11-0796.
1088